Universal Kinetics of the Thermal Decomposition of Synthetic Smithsonite over Different Atmospheric Conditions

Nobuyoshi Koga, Yasuhiro Sakai, Masahiro Fukuda, Daichi Hara, Yuu Tanaka, Loïc Favergeon

Universal Kinetics of the Thermal Decomposition of Synthetic Smithsonite over Different Atmospheric Conditions

Nobuyoshi Koga,[a,*] Yasuhiro Sakai,[a] Masahiro Fukuda,[a] Daichi Hara,[a] Yuu Tanaka,[a] Loic Favergeon[b]

[a] Department of Science Education, Graduate School of Education, Hiroshima University, 1-1-1 Kagamiyama, Higashi-Hiroshima 739-8524, Japan

[b] Mines Saint-Etienne, University of Lyon, CNRS, UMR 5307 LGF, Centre SPIN, F-42023 Saint-Etienne, France.

Abstract

The thermal decomposition of smithsonite ($ZnCO_3$) was studied to obtain a universal kinetic description of the process applicable to a range of reaction conditions. A synthesized $ZnCO_3$ was subjected to thermoanalytical measurements under various heating and atmospheric conditions in a flow of dry N_2 gas, N_2–CO_2, or N_2–H_2O mixed gases. Systematic shifts of the reaction temperature to higher and lower temperatures by the effects of CO_2 and H_2O, respectively, were identified as specific characteristics of the system. With reference to the physico-geometrical kinetic behavior of the reaction in a flow of dry N_2 gas, the retardation effect of CO_2 was demonstrated in the scheme of the physico-geometrical consecutive surface reaction (SR) and phase boundary-controlled reaction (PBR). The individual kinetics of the SR and PBR were universally described over different CO_2 pressures using an accommodation function (AF) obtained by considering the consecutive elementary steps of SR and PBR. The catalytic effect of water vapor was assumed to result from contributions of the water molecules on the consecutive elementary steps of SR and on the crystal growth of the solid product of the reaction (ZnO). An alternative AF derived considering the adsorption of water molecules on solid surfaces allowed us to obtain the universal kinetic description of the thermal decomposition over different water vapor pressures.

1. Introduction

The thermal decomposition of metal carbonates is significantly influenced by the evolved gas CO_2. In fact, the influence of atmospheric CO_2 on the described class of processes has been studied for nearly a century.[1-16] In general, atmospheric CO_2 has a retardation effect on the kinetics of the mentioned thermal decomposition. Thus, the kinetic characterization of the thermal decomposition should be considered as including a determination of the influence that the partial pressure of CO_2 ($p(CO_2)$ in kPa) has on it, in

addition to the changes in the reaction rate as a function of reaction temperature (T) and the fraction reaction (α). When considering the effect of $p(CO_2)$, the reaction equilibrium characterized by the equilibrium CO_2 pressure ($P_{eq}(T)$ in atm) at each temperature should also be taken into account.[1-13, 17-18] The generalized reaction rate ($d\alpha/dt$) is expressed by multiplying functions expressing the dependencies on T, α, and $p(CO_2)$.[18-23]

$$\frac{d\alpha}{dt} = A\exp\left(-\frac{E_a}{RT}\right)f(\alpha)h\left(p(CO_2), P_{eq}(T)\right) \tag{1}$$

where A and E_a are the apparent values of the Arrhenius preexponential factor and activation energy, respectively. R is the gas constant. The function $f(\alpha)$ is the kinetic model function, which describes the variation of kinetic behavior at a constant temperature as the reaction advances. The function labeled $h(p(CO_2), P_{eq}(T))$ is interpreted as an accommodation function (AF)[24-29] introduced into the fundamental kinetic equation to account for the effect of $p(CO_2)$ value. Ideally, eq. 1 provides a universal kinetic description of the thermal decompositions of carbonates over different temperature and $p(CO_2)$ conditions, for which the $h(p(CO_2), P_{eq}(T))$ plays an indispensable role in obtaining a universal kinetic description. The most frequently used form of $h(p(CO_2), P_{eq}(T))$ is expressed by:[2, 4, 9, 11, 17]

$$h\left(p(CO_2), P_{eq}(T)\right) = 1 - \frac{p(CO_2)}{P°P_{eq}(T)} \tag{2}$$

where $P°$ in kPa is the standard pressure introduced to normalize the pressure unit of ($\frac{p(CO_2)}{P°}$) to be atm. Eq. (2) was obtained on the basis of various theoretical considerations.[4-5, 9, 17, 30] The practical application of eq. (1) accompanied by eq. (2) corrects the slope of the Arrhenius-type plots at each $p(CO_2)$ value; however, the kinetics is not necessary described successfully by a single Arrhenius-type plot over different $p(CO_2)$ values.[11, 20-23] Accordingly, theoretical and experimental resolutions of the universal kinetic description for the thermal decomposition of metal carbonates over different temperature and $p(CO_2)$ conditions are the current challenge for gain further insight into the kinetics of the thermal decomposition of solids.[20-23]

Another concern with respect to the kinetics of the thermal decomposition of metal carbonates is the effect of atmospheric water vapor. Acceleration effects of atmospheric water vapor have been reported for the thermal decompositions of several metal carbonates,[16,31-35] including $CaCO_3$.[36-44] Notably, a catalytic effect of atmospheric water vapor has also been observed for the reverse reactions, i.e., the carbonation of metal oxides including ZnO,[45,46] CaO,[47,48] and MgO.[49-51] Since the mentioned acceleration effects of water vapor on the thermal decomposition of metal carbonates and the carbonation of metal oxides allow for the reaction temperatures to be reduced, these phenomena have received much attention in the evaluation of CO_2 absorption and energy storage via metal carbonate-metal oxide looping system.[52-54] In view of the chemical mechanism of the thermal decomposition of carbonates, the catalytic effect of water vapor has been explained by considering the contribution of water molecules to the elementary steps of the overall process at the reaction interface via the possible formation of hydrogen carbonate ions as intermediates.[43,44] Conversely, the thermal decomposition of solids is a heterogeneous

process, which is significantly constrained by physicogeometrical factors and mass and heat transfer phenomena.[26,29,55,56] In the scheme of a core-shell structure of reactant and product solids during the said reactions, water vapor alters the overall reaction rate as a result of its effect on the growth of the product crystals in the surface product layer because of the changes in the diffusion path of the gaseous product via the surface product layer. Accelerations of the crystal growth and sintering of metal oxides by atmospheric water vapor have also been reported for ZrO_2,[57,58] MgO,[59-61] and TiO_2.[62] Therefore, the acceleration effect of atmospheric water vapor on the thermal decomposition of solids should be interpreted as resulting from both the chemical process occurring at the reaction interface and the physicogeometrical features of the reaction interface advancement. Notably, atmospheric CO_2 and water vapor have been observed to have opposite effects on the thermal decomposition of metal carbonates and carbonate hydroxides, such as $Cu_2CO_3(OH)_2$[31-34,63] and $Zn_5(CO_3)_2(OH)_6$.[16,35,64] In these types of reactions, the kinetic effects of atmospheric CO_2 and water vapor should be interpreted comparatively as a way to understand the kinetic behavior over different temperature and atmospheric conditions. In our preliminary investigation for the present study, the thermal decomposition of $ZnCO_3$ to form ZnO was found to be an example of a reaction for which atmospheric CO_2 and water vapor have opposite kinetic effects. Notably, acquiring detailed kinetic information on this reaction is especially desirable, given the various potential applications of ZnO, which is characterized as an n-type semiconductor.[65] Thus, a detailed kinetic understanding of the mentioned process may contribute to achieving a sophisticated control the reaction process and the morphological and physical properties of its solid product, i.e., ZnO. $ZnCO_3$ is found in nature in the form of the mineral smithsonite.[66-68] The kinetics of the thermal decomposition of smithsonite has been studied in vacuum:[69,70] evidence revealed a deceleration of the reaction rate as the reaction advanced. Single-phase $ZnCO3$ has been successfully synthesized by Hales and Frost applying the hydrothermal treatment to a mixed solution of $ZnCl_2$ and $NaHCO_3$ in aqueous solution.[71] The thus-obtained synthetic smithsonite has been structurally characterized and investigated in thermoanalytical studies.[72,73] However, the influence of atmospheric $p(CO_2)$ on the kinetics of the thermal decomposition has not been studied in detail. In addition, little attention has been paid to the effect that atmospheric water vapor has on the said process. The present study aims to elucidate the physicochemical kinetic behaviors of the thermal decomposition of metal carbonates across different atmospheric CO_2 and water vapor conditions using the thermal decomposition of $ZnCO_3$ as a model process for the described reaction type. To face the challenge of achieving a kinetic understanding of the thermal decomposition of solids, a systematic experimental approach was undertaken in a stepwise manner: (1) laboratory synthesis of $ZnCO_3$ crystalline powders and their characterization, (2) formal kinetic characterization of the thermal decomposition under inert gas atmosphere, (3) universal kinetic description of the thermal decomposition under various atmospheric $p(CO_2)$ conditions, and (4) universal kinetic description of the thermal decomposition under various atmospheric water vapor pressure ($p(H_2O)$ in kPa) conditions. In each step of the inquiry, novel features of the material and its thermal decomposition process were revealed via the collection of

extensive experimental data, followed by the performance of detailed kinetic analyses implementing conventional and advanced methods. The physicogeometrical kinetic description of the thermal decomposition of $ZnCO_3$ under different temperature, $p(CO_2)$, and $p(H_2O)$ conditions was then realized by integrating the novel findings of the present study.

2. EXPERIMENTAL SECTION

2.1. Preparation and Characterization of the Precursor and $ZnCO_3$ Sample.

A mixed precipitation of $ZnCO_3$ and hydrozincite $(Zn_5(CO_3)_2(OH)_6)$[16,35,64] was used as the precursor for preparing crystalline zinc carbonate with the crystal structure of the mineral smithsonite. The precursor was subjected to repeated hydrothermal treatments in an aqueous solution of sodium hydrogen carbonate (Figures S1-S6). The precursor materials, as well as the hydrothermally treated products, were characterized by powder X-ray diffractometry (XRD), Fourier transform infrared (FT-IR) spectroscopy, and simultaneous thermogravimetry (TG)-differential thermal analysis (DTA). The morphology of the hydrothermally treated product was observed by scanning electron microscope (SEM). Detailed preparation procedures and characterizations are described in Sections S1.1 and S2.1 in the Supporting Information for the precursor materials and hydrothermally treated products, respectively.

2.2. Thermal Behavior of the Sample.

A characterized $ZnCO_3$ sample of approximately 2.0 mg (initial sample mass (m_0)), weighed in an open platinum pan (diameter, 5 mm; height, 2.5 mm), was subjected to TG-DTA measurements in a flow of He gas (flow rate = 200 cm^3 min^{-1}) using a TG8120 instrument (Thermoplus 2 system, Rigaku Co.). The sample was heated at a heating rate (β) of 5 K min^{-1} from 293 to 973 K. During the TG-DTA measurement, a portion of the outlet gas was continuously transferred to a quadrupole mass spectrometer (MS; M-200QA, ANELVA) via a silica capillary tube (internal diameter, 0.075 mm; length, 0.7 m) heated at a constant temperature of 500 K. The mass spectra of the outlet gas were repeatedly measured with no interval time in an m/z range of 10-50 amu (EMSN: 1.0 mA; SEM: 1.0 kV). Changes in the XRD pattern of the sample as it was being heated under a dry N2 gas flow (flow rate = 100 cm^3 min^{-1}) were traced according to two different heating programs. In one such program, the sample, press-fitted to a platinum plate, was heated at β = 10 K min^{-1}; during heating, isothermal holding sections for each 15 min were inserted at every 25 K in the temperature range from 473 to 773 K (stepwise isothermal heating). XRD measurements were conducted during each isothermal holding section under conditions otherwise identical to those applied to the sample characterization (see Section S1.1 in the Supporting Information). Another set of high-temperature XRD measurements were carried out under isothermal conditions at 538 K after the sample had been heated linearly at β = 10 K min^{-1} to 538 K (isothermal heating). XRD measurements were repeated every 15 min for 5 h. High-temperature XRD measurements were also carried out in a flow of N_2-H_2O mixed gas (relative humidity: 80% at 298 K) and N_2-CO_2 mixed gas ($p(CO_2)$ = 40 kPa) under conditions that were otherwise identical to those

described for the experiment carried out under dry N_2 gas flow condition. A characterized $ZnCO_3$ sample of approximately 400 mg was weighed into an alumina boat (SSA-A; width, 13.5 mm; length, 30 mm; depth, 10 mm). Such a sample was then heated linearly at $\beta = 2$ K min^{-1} to different temperatures ranging from 423 to 873 K under dry N_2 gas flow conditions (flow rate = 100 cm^3 min^{-1}) using a tube furnace (Isuzu Seisakusho). The heat-treated sample was then cooled in the furnace under N_2 gas flow and then recovered from the furnace and subjected to FT-IR and specific surface area measurements. The FT-IR spectra of the series of heat-treated samples were measured implementing the same procedures applied for sample characterization (see Section S1.1 in the Supporting Information). For the specific surface area measurement, approximately 200 mg of each heat-treated sample was weighed into a glass tube cell and degassed at 373 K for 30 min in a flow of N_2-He mixed gas (N_2: 30.1%; He: balance). Subsequently, the specific surface area was measured using a FlowSorb 2300 II instrument (Micromeritics) employing the Brunauer-Emmett-Teller (BET) single-point method.[74]

2.3. Measurement of Kinetic Curves.

To track the kinetic behavior of the thermal decomposition of $ZnCO_3$, the mass-loss traces during the reactions were recorded under different atmospheric conditions in a flow of dry N_2 gas, N_2-CO_2 mixed gas with different $p(CO_2)$ values, and N_2-H_2O mixed gas with different $p(H_2O)$ values. The measurements in a flow of dry N_2 and N_2-CO_2 mixed gas were conducted with a TG-DTA instrument (TG-8121, Thermoplus Evo2 system, Rigaku). By contrast, a humidity-controlled TG-DTA system (HUM-TG, Thermoplus 2 system, Rigaku) was used for the measurements conducted in a flow of N_2-H_2O mixed gas. Approximately 5.00 mg of the sample, weighed in a platinum open cell (diameter, 5 mm; height, 2.5 mm), were used for all of the measurements. In addition, measurements under three different temperature program modes, i.e., isothermal, linear nonisothermal, and controlled transformation rate thermal analysis (CRTA),[75,76] were applied to the collection of the mass-loss traces under the various atmospheric conditions. In the case of the measurements conducted in a flow of dry N_2 gas, the applied flow rate was 300 cm^3 min^{-1}. The sample was heated at a β value of 10 K min^{-1} to a programmed temperature in the $539 \leq T/K \leq 564$ range and held the temperature during the mass-loss process of the thermal decomposition (isothermal mode). The mass-loss traces under linear nonisothermal conditions were recorded by heating the sample from room temperature to 773 K applying various β values in the $0.5 \leq \beta/K$ min$^{-1} \leq 3$ range. For the CRTA measurements, the sample was heated at a β of 2 K min^{-1}, while, during the mass-loss process, the sample temperature was regulated to maintain the programmed constant mass-loss rate (C) in the $2.5 \leq C/\mu g$ min$^{-1} \leq 20$ range. The N_2-CO_2 mixed gas was prepared by mixing dry N_2 and CO_2 gases in an anterior chamber; the gas was then introduced into the furnace tube of the TG-DTA instruments at a rate of 300 cm^3 min^{-1}. The outlet gas from the furnace tube was transferred to a CO_2 meter (LX-710, IIJIMA), which allowed the $p(CO_2)$ value in the N_2-CO_2 mixed gas to be continuously monitored. The $p(CO_2)$ value was controlled by changing the flow rates of dry N_2 and CO_2, which in turn affected the ratio of these two gases. To

evaluate the influence that the $p(CO_2)$ value had on the mass-loss trace, the sample was heated linearly at $\beta = 5$ K min-1 from room temperature to 873 K in a flow of N2-CO2 mixed gases characterized by different $p(CO_2)$ values ($5 \leq p(CO_2)/kPa \leq 80$). Four $p(CO2)$ values were selected, that is 5, 10, 20, and 40 kPa, and a series of mass-loss traces were recorded under isothermal, linear nonisothermal, and CRTA conditions at each $p(CO_2)$ value. The mass-loss traces under isothermal conditions were recorded in the $588 \leq T/K \leq 613$, $598 \leq T/K \leq 623$, $613 \leq T/K \leq 638$, and $624 \leq T/K \leq 644$ temperature ranges for the reactions conducted in a flow of N$_2$- CO$_2$ mixed gases characterized by $p(CO_2)$ values of 5, 10, 20, and 40 kPa, respectively. The measurements under linear nonisothermal and CRTA conditions were carried out using identical heating parameters to those described above for the measurements in a flow of dry N$_2$ gas, although the maximum value for the programmed temperature was 873 K. To draw the mass-loss traces of the samples in a flow of N$_2$-H$_2$O mixed gas characterized by different $p(H_2O)$ values, the samples were initially heated to 353 K at $\beta = 10$ K min^{-1} in a flow of dry N$_2$ gas at a rate of 400 cm^3 min^{-1}. Immediately after the sample temperature reached 353 K, the flowing gas was switched to N$_2$-H2O mixed gas with a controlled $p(H_2O)$ value, as determined by a humidity controller (HUM-1, Rigaku).[77] In a flow of N$_2$-H$_2$O mixed gas at a rate of 400 cm^3 min^{-1}, the measurement system was stabilized by holding the sample temperature at 353 K for 30 min. Thereafter, the sample was heated from 353 to 673 K at a rate of $\beta = 5$ K min^{-1}, so as to obtain mass-loss curves in a flow of N$_2$-H$_2$O mixed gases with different $p(H_2O)$ values in the $0.81 \leq p(H_2O)/kPa \leq 11.0$ range. At the selected $p(H_2O)$ value of 9.56 kPa, the mass-loss traces were measured under isothermal, linear nonisothermal, and CRTA mode conditions. The isothermal mass-loss traces were recorded at different temperatures in the $454 \leq T/K \leq 494$ range. The measurements under linear nonisothermal conditions were carried out by heating the sample from 353 to 673 K at different β values in the $0.5 \leq \beta/K$ min$^{-1} \leq 3$ range. In the CRTA measurements, the programmed C value was made to vary in the $10 \leq C/\mu g$ min$^{-1} \leq 30$ range.

2.4. Morphology of the Reacting Particles.

The ZnCO$_3$ samples were made to react partially at different α values in each atmospheric condition: in a flow of dry N$_2$ gas, N$_2$-CO$_2$ mixed gas, or N$_2$-H$_2$O mixed gas. Approximately 10 mg aliquots of samples were heated at a rate of $\beta = 5$ K min^{-1} to different final temperatures under conditions that were otherwise identical to those utilized to carry out the measurements of kinetic curves in each atmospheric condition. Controlled values of 40 and 9.44 kPa were selected for $p(CO_2)$ and $p(H_2O)$ for the preparations of partially reacted samples in a flow of N$_2$-CO$_2$ and N$_2$-H$_2$O mixed gases, respectively. The as-prepared samples were immediately cooled to room temperature and subjected to SEM (JSM-6510, JEOL) observations after being coated with a thin platinum layer by way of sputtering (JFC-1600, JEOL, 30 mA, 30 s) as in the procedure described previously (see Section S2.1 in the Supporting Information).

3. RESULTS AND DISCUSSION

3.1. Characterization of Sample.

The procedures implemented for the synthesis and characterization of smithsonite are detailed in Section S2.1 in the Supporting Information. By repeating the hydrothermal treatment of the precursor, which comprised a mixture of hydrozincite and smithsonite, in 0.5 M-NaHCO$_3$(aq) at 373 K for each 6 h, the hydrozincite phase was gradually transformed into smithsonite. After conducting the hydrothermal treatment four consecutive times, no hydrozincite was detected in the sample by XRD, FT-IR, and TG-derivative TG (DTG) (Figures S4-S6). The XRD pattern of the as-produced sample was a perfect match to that reported for smithsonite (ZnCO$_3$, trigonal, S.G.: R$\overline{3}$c(167), a = b = 4.6533, c = 15.0280, α = β = 90.000, γ = 120.000, ICDD PDF 00-008-0449).[78,79] TG-DTG curves exhibited a well-shaped single-step mass-loss curve during the thermal decomposition of the as-produced sample (Figure S6), which indicated an average mass-loss ratio of 35.7 ± 0.6%, a value very close to that calculated for the relative mass-loss associated with the thermal decomposition of ZnCO$_3$ (35.1%; eq 3).

$$ZnCO_3(s) \rightarrow ZnO(s) + CO_2(g), \; \Delta_r H_{298} = 80.0 \text{ kJ mol}^{-1} \qquad (3)$$
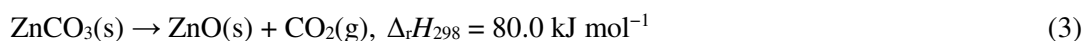
The ZnCO$_3$ sample obtained after performing the hydrothermal treatment four consecutive times was an agglomerate of polyhedral crystals with well-developed crystal faces of sizes ranging from 1 to 5 μm (Figure S7) with the BET specific surface area (S$_{BET}$) value of 0.57 ± 0.05 cm^2 g^{-1}.

3.2. Thermal Behavior of the As-Prepared ZnCO$_3$ Sample.

Figure 1 reports the TG-DTA curves for the thermal decomposition of the ZnCO$_3$ sample in a flow of He (flow rate, 200 cm^3 min^{-1}), together with the MS chromatograms for the species with m/z = 18 (H$_2$O$^+$) and 44 (CO$_2^+$) of the evolved gas. This evidence indicates that the only gas evolved during the mass-loss process associated with the endothermic thermal decomposition of the ZnCO$_3$ sample was CO$_2$. No detectable amounts of water vapor, which would result from the thermal decomposition of hydrozincite, were observed to be present in the evolved gas.
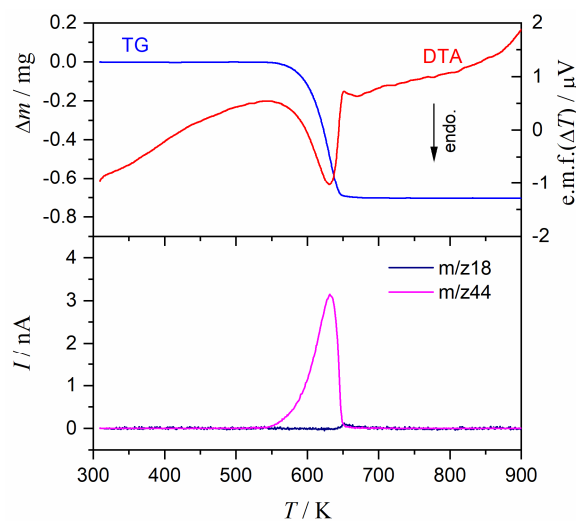

Figure 1. Typical TG/DTA-MS traces for the thermal decomposition of the ZnCO$_3$ sample.

Changes in the XRD pattern of the $ZnCO_3$ sample as a result of being subjected to heating in a flow of dry N_2 gas as part of experiments conducted under stepwise isothermal and isothermal heating conditions are reported in Figures S8 and S9, respectively. In the stepwise isothermal heating mode, the thermal decomposition of $ZnCO_3$ occurred within the 523-598 K temperature range. In fact, as the sample temperature increased in the temperature range, the XRD peaks attributed to $ZnCO_3$ gradually attenuated, a phenomenon accompanied by the gradual growth of the peaks attributed to the solid product (Figure S8a). The XRD pattern of the solid product corresponded to that reported for ZnO (hexagonal, S.G. = P63mc (186), a = b = 3.2535, c = 5.2151, $\alpha = \beta = 90.000$, $\gamma = 120.000$, ICDD PDF 01-080-0074)[80] (Figure S8b), and no distinguishable XRD peaks due to a crystalline intermediate were observed during the thermal decomposition. The average ZnO crystallite size estimated applying the Scherrer equation,[81] with reference to (1,0,0), (0,0,2), (1,0,1), and (1,1,0), appeared at 2θ of 31.7, 34.4, 36.2, and 56.5°, respectively, was ~9 nm within the temperature range of the thermal decomposition (Figure S8c); the value of this parameter subsequently increased linearly to approximately 23 nm as the temperature increased to 773 K. Under isothermal conditions at 538 K, the thermal decomposition of $ZnCO_3$ was observed to be complete after 135 min (Figure S9a), and the solid product was observed to consist exclusively of ZnO (Figure S9b). The value for the ZnO crystallite size was approximately 9 nm during the thermal decomposition, and this value did not increase significantly upon continuously heating the sample further at 538 K after the thermal decomposition was completed (Figure S9c). Figure S10 shows the data reflecting the changes in the XRD pattern of the $ZnCO_3$ sample during the stepwise isothermal heating in a flow of N_2-CO_2 (p(CO_2) = 40 kPa) and N_2-H_2O (p(H_2O) $\cong$ 2.5 kPa) mixed gases. The thermal decomposition of $ZnCO_3$ to form ZnO was observed to occur in the 573-648 and 498-598 K temperature ranges in the N_2-CO_2 and N_2-H_2O atmospheres, respectively. In comparison to the process that took place in a flow of dry N_2 gas, the presence of CO_2 and H_2O gases in the reaction atmosphere caused the decomposition temperature range to shift to higher and lower values, respectively. The values of the observed ZnO crystallite sizes determined upon heating the sample in different gaseous atmospheres are shown in Figure S11. In comparison to the growth behavior of ZnO crystallites in a dry N_2 atmosphere, a large delay was observed during the thermal decomposition in the presence of atmospheric CO_2, which is a relevant species in the standpoint of the reaction equilibrium of the thermal decomposition of $ZnCO_3$ (see eq 3). By contrast, a detectable acceleration was evident for the thermal decomposition carried out in the presence of water vapor. The crystallite size of ZnO heated to 773 K decreased in the following order, depending on the composition of the reaction atmosphere: N_2-H_2O (27.6 ± 3.1 nm) > dry N_2 (23.5 ± 0.8 nm) > N_2-CO_2 (18.9 ± 1.6 nm). Figure 2 shows the TG-DTA curves recorded in the different atmospheric conditions. Apparent shifts of the TG-DTA curves to higher and lower temperatures as a result of the presence of CO_2 and H_2O, respectively, in the reaction atmosphere were confirmed as specific characteristics of the thermal decomposition of $ZnCO_3$.
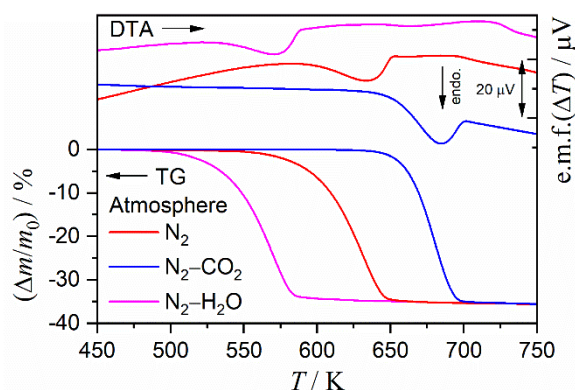
Figure 2. Comparison of the TG–DTA curves for the ZnCO$_3$ sample (m_0: approximately 5.0 mg) recorded under linear nonisothermal condition at β of 5 K min^{-1} in different atmospheric conditions of a flow of dry N$_2$, N$_2$–CO$_2$ (p(CO$_2$) = 40 kPa), and N$_2$–H$_2$O (p(H$_2$O) = approx. 2.8 kPa) gases.

The changes in FT-IR spectra of the ZnCO$_3$ samples heated to different temperatures are reflected by the data in Figure S12. In the FT-IR spectrum of the thermally treated ZnCO$_3$ sample, the thermal decomposition of ZnCO$_3$ to form ZnO at the treated temperature values of 573 and 623 K was clearly indicated by the disappearance of the absorption peaks attributed to the ν_2, ν_3, and ν_4 modes of CO$_3^{2-}$, which were observed at 870, 1474, and 744 cm^{-1} wavenumbers, respectively.[66,71] Figure S13 reports the data reflecting the changes in the S$_{BET}$ value of the preheated samples. Notably, a dramatic increase in the S$_{BET}$ value was observed between the samples heated to 523 and 623 K, which correspond to the reaction temperature range of the thermal decomposition of ZnCO$_3$ as observed previously in the TG/DTA-MS (Figure 1), XRD (Figures S8 and S9), and FT-IR (Figure S12) analyses.

3.3. Thermal Decomposition of ZnCO$_3$ in a Dry N$_2$ Atmosphere.

Figure 3 shows the TG-DTG curves for the thermal decomposition of the ZnCO$_3$ sample under isothermal, linear nonisothermal, and CRTA conditions in a flow of dry N$_2$ gas. Those TG-DTG curves were converted to individual kinetic curves composed of data point series (time, T, α, dα/dt) by defining α normalized ⟨0, 1⟩ with reference to the total mass-loss value for the thermal decomposition. The kinetic curves configured in three-dimensional coordinates of time-T-α and time-T-(dα/dt) show a wide range of time- T-α-(dα/dt) covered by the kinetic data recorder under isothermal, linear nonisothermal, and CRTA conditions (Figure S14).
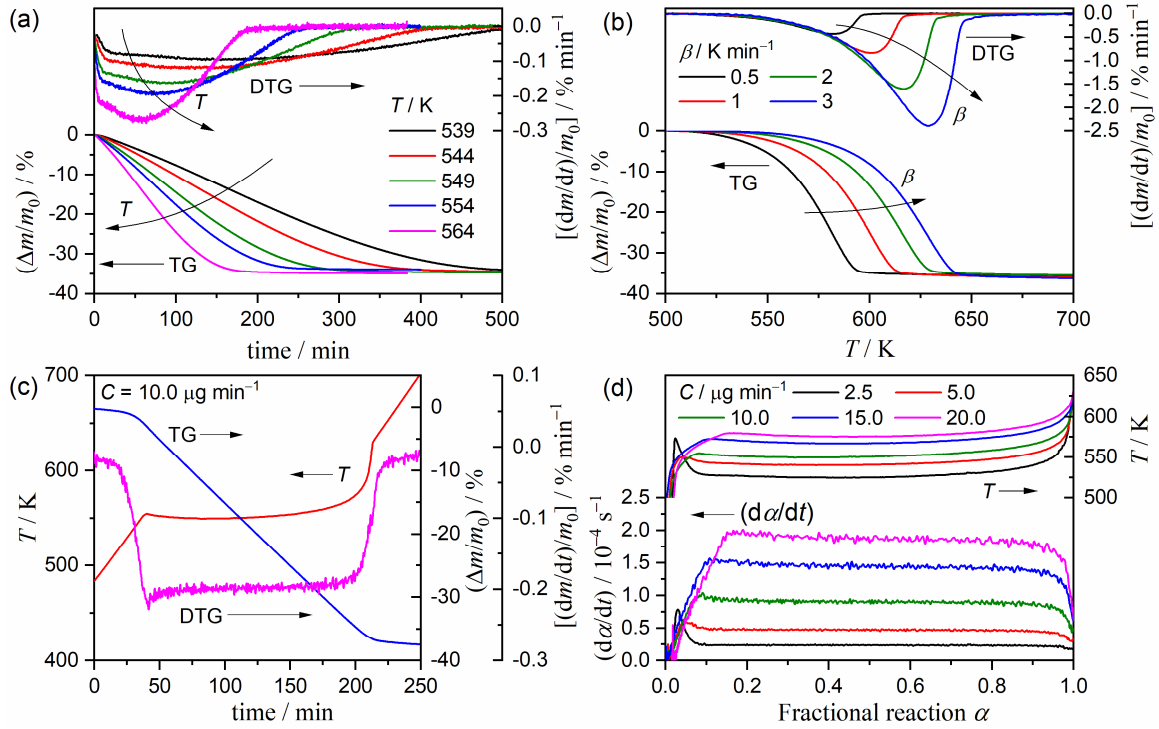
Figure 3. TG–DTG curves for the thermal decomposition of the $ZnCO_3$ sample recorded in a dry N_2 gas flow (flowrate: 300 cm³ min⁻¹) under various heating conditions: (a) isothermal conditions ($m_0 = 5.004 \pm 0.026$ mg), (b) nonisothermal conditions ($m_0 = 4.966 \pm 0.057$ mg), (c) typical CRTA record, and (d) changes in sample temperature and reaction rate ($d\alpha/dt$) during the reaction under CRTA conditions ($m_0 = 5.009 \pm 0.022$ mg).

These kinetic data were simultaneously subjected to the kinetic calculation based on the fundamental kinetic equation for solid-state reactions[27-29]

$$\frac{d\alpha}{dt} = A\exp\left(-\frac{E_a}{RT}\right)f(\alpha) \tag{4}$$

By taking the logarithm of eqs 4, we obtain 5

$$\ln\left(\frac{d\alpha}{dt}\right) = \ln\left[Af(\alpha)\right] - \frac{E_a}{RT} \tag{5}$$

The isoconversional section of the kinetic relation is represented by the linear correlation between $\ln(d\alpha/dt)$ and T^{-1}, given that $\ln[Af(\alpha)]$ is a constant at a given value for α. The isoconversional kinetic relationship was examined for all of the kinetic data as $\ln(d\alpha/dt)$ versus T^{-1} plots at various α values (Friedman plot[82]) can be evinced from Figure 4. Irrespective of the heating conditions and α value, the isoconversional kinetic relationship was established to be characterized by a statistically significant linear correlation at each α (Figure 4a). The slopes of the plots at different α values were approximately constant within the $0.1 \leq \alpha \leq 0.9$ range. The trend in variation of the slope as the reaction advances is viewed in more detail as the variation of E_a calculated from the slope of the Friedman plot, i.e., $-E_a/R$ (Figure 4b). Through the main reaction stage ($0.1 \leq \alpha \leq 0.9$), E_a remained quite constant, displaying an average value of 104.7 ± 2.9 kJ mol⁻¹; however, a detectable decrease in E_a value from approximately

140 to 105 kJ mol^{-1} was observed in the initial part of the reaction ($\alpha \leq 0.1$), although the statistical significance of the linear correlation of the Friedman plot was maintained also at this stage of the reaction. Notably, a drastic drop in the E_a value is also observed in the final stage of the reaction ($\alpha \geq 0.95$), but this change was likely due to the specific characteristics of reaction tail, where the variation in the reaction rate with the heating condition is not so significant. Assuming the occurrence of a single-step reaction characterized by a constant E_a value, the hypothetical reaction rate ($d\alpha/d\theta$) at infinite temperature was calculated at different α values using the following equation[32,83-87]

$$\frac{d\alpha}{d\theta} = \left(\frac{d\alpha}{dt}\right) \exp\left(\frac{E_a}{RT}\right) = Af(\alpha) \qquad \text{with} \qquad \theta = \int_0^t \exp\left(-\frac{E_a}{RT}\right) dt \qquad (6)$$

where θ is Ozawa's generalized time,[88,89] which denotes the hypothetical reaction time at infinite temperature. The plot of $d\alpha/d\theta$ versus α (Figure 4b) is also correlated to $f(\alpha)$ according to eq 6, which is thus used to evaluate $f(\alpha)$ and A value as the experimental master plot. The experimental master plot exhibited the maximum rate midway through the reaction.

With reference to the physicogeometrical kinetic model for the thermal decomposition of solids,[26,55,56] which includes surface reaction (SR) followed by shrinkage of the reaction interface toward the center of reactant particle, the increase in reaction rate in the first half of the reaction points to a contribution of the SR to the overall reaction. The decrease in the isoconversional E_a value in the initial part of the reaction also supports the mentioned inference. Because other physicogeometrical kinetic models for single-step reactions did not show any relevant fits to the experimental master plot, the overall reaction process was empirically fitted by the Šesták-Berggren model, SB(m, n, p):[24,90,91]

$$SB(m, n, p): f(\alpha) = \alpha^m (1-\alpha)^n [-\ln(1-\alpha)]^p \qquad (7)$$

The empirical A value of $(8.56 \pm 0.09) \times 10^5$ s^{-1} was obtained by fitting the experimental master plot with SB(-2.19, 1.35, 2.33), whereby a determination coefficient, R^2, equal to 0.9985 was determined.
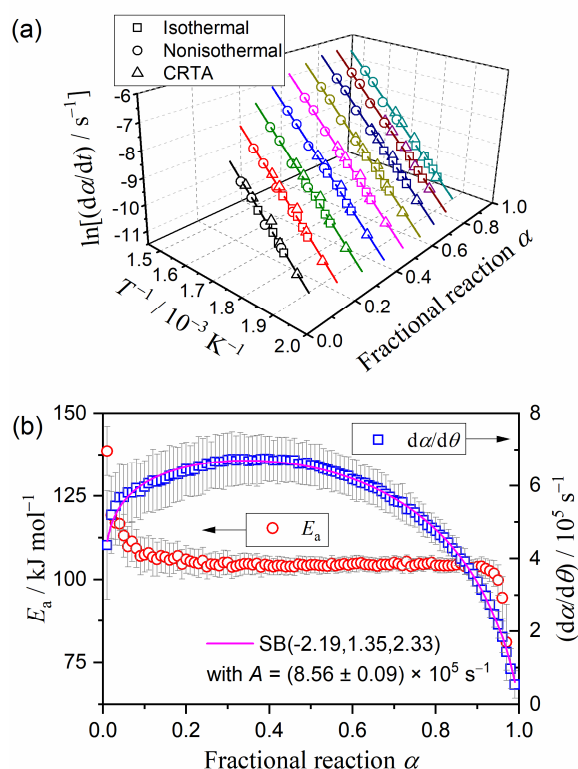
Figure 4. Results of the isoconversional kinetic analysis for the thermal decomposition of the $ZnCO_3$ sample in a flow of dry N_2: (a) Friedman plots at various α values from 0.1 to 0.9 in steps of 0.1, (b) E_a values at various α, and (c) experimental master plot of $d\alpha/d\theta$ versus α and the fit curve using SB(m, n, p).

In spite of the nearly perfect fit obtained, the kinetic exponents in SB(m, n, p) cannot have any relevant physicochemical meanings for describing the physicogeometrical reaction mechanism of the thermal decomposition of $ZnCO_3$ because the physicogeometrical consecutive process composed of SR and subsequent contracting geometry-type processes were fitted by assuming a single-step reaction. Even so, the optimized kinetic exponents can be used for the formal description of the overall rate behavior. SEM photographs of the partially decomposed $ZnCO_3$ samples characterized by different α values, which had been obtained by subjecting the samples to linear heating at β = 5 K min⁻¹ to different final temperatures in a flow of dry N_2 gas, are shown in Figure S15. Although the particle shapes did not change significantly during thermal decomposition, an increase in the roughness of the particle surfaces was evident in the early stage of the reaction. This observation also supports the geometrical reaction model characterized by SR and subsequent shrinkage of the reaction interface.

3.4. Thermal Decomposition of $ZnCO_3$ in N_2-CO_2 Atmosphere.

Figure 5 shows the TG-DTG curves of the $ZnCO_3$ samples recorded nonisothermally at β = 5 K min⁻¹ in a flow of N_2-CO_2 mixed gases characterized by different p(CO_2) values. The mass-loss curves shifted systematically to higher temperatures as the values of p(CO_2) increased (Figure 5a). The shapes of TG-

DTG curves appeared different, depending on whether CO_2 was present in the reaction atmosphere or not. By contrast, the said shapes were not significantly influenced by the $p(CO_2)$ value, as can be evinced from the approximately constant temperature interval between the extrapolated onset (T_{eo}) and peak top (T_p) temperatures, and the approximately constant maximum height of the DTG peak in the experiments conducted at $p(CO_2)$ values above 10 kPa (Figure 5b).
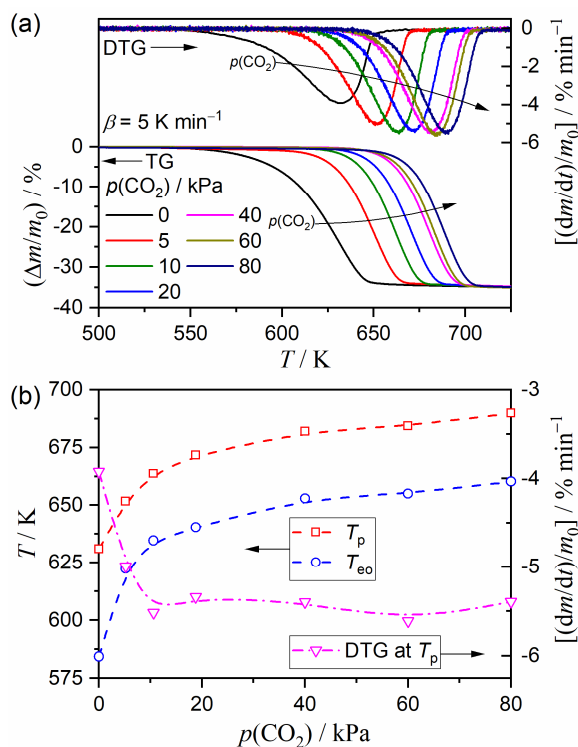

Figure 5. TG–DTG curves for the thermal decomposition of the $ZnCO_3$ sample ($m_0 = 5.056 \pm 0.103$ mg) recorded at $\beta = 5$ K min^{-1} in a flow of N_2–CO_2 mixed gas with different $p(CO_2)$ values (flowrate: 300 cm^{3}min^{-1}).

Figure 6 shows the TG-DTG curves for the thermal decomposition of $ZnCO_3$ samples recorded in a flow of N_2-CO_2 mixed gases characterized by a $p(CO_2)$ value of 10 kPa under different heating conditions. Notably, the TG-DTG curves recorded at different $p(CO_2)$ values (5, 10, 20, and 40 kPa) in each heating condition are shown in Figures S16-S19: isothermal (Figure S16), linear nonisothermal (Figure S17), and CRTA (Figures S18 and S19). The characteristics of this series of TG-DTG curves are described in Supporting Information S5. At each $p(CO_2)$ value, the kinetic curves obtained from the conversion of the TG-DTG curves recorded under different heating conditions cover various paths in the time-T-α and time-T-dα/dt coordinates, as can be evinced from Figures S20-S23, whereby are reported data for the reactions occurring at different $p(CO_2)$ values.

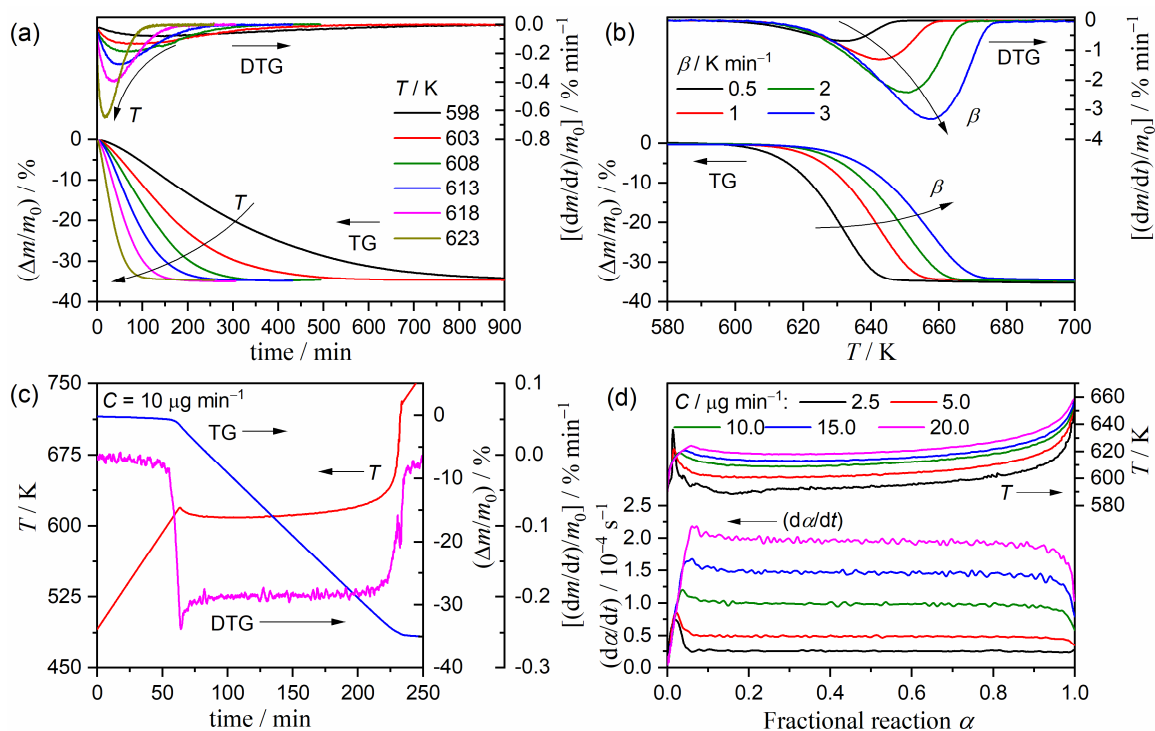**Figure 6.** TG–DTG curves for the thermal decomposition of the $ZnCO_3$ sample recorded in a N_2–CO_2 mixed gas flow ($p(CO_2) = 10$ kPa; flowrate: 300 cm^3 min^{-1}) under various heating conditions: (a) isothermal conditions (m_0 = 4.975 ± 0.074 mg), (b) nonisothermal conditions (m_0 = 4.939 ± 0.098 mg), (c) typical CRTA record, and (d) changes in sample temperature and reaction rate ($d\alpha/dt$) during the reaction under CRTA conditions (m_0 = 4.975 ± 0.062 mg).

The kinetic data recorded in different heating conditions at each $p(CO_2)$ value were initially analyzed via the conventional isoconversional method without considering the effect of atmospheric $p(CO_2)$ values. Figure 7 summarizes the results of the conventional kinetic analysis. Irrespective of the $p(CO_2)$ value, the Friedman plot at a given $p(CO_2)$ value exhibited a statistically significant linear correlation (Figure 7a), which was observed at different α values during the reaction (see Figure S24). However, different linear correlations were evident for the reactions conducted under different $p(CO_2)$ values; in fact, the slope of the plots increased with $p(CO_2)$ value. Comparisons of the calculated E_a values at various α values among the reactions at different $p(CO_2)$ values clearly indicate that the apparent E_a values increased as the $p(CO_2)$ values increased (Figure 7b). The variation trend of the E_a value as the α value increased also differed among the reactions conducted under different $p(CO_2)$ values. Although the E_a values were approximately constant for each $p(CO_2)$ value through the main part of the reaction (0.20 ≤ α ≤ 0.90), the variation trends of E_a switched systematically in the initial part of the reaction (0.01 ≤ α ≤ 0.20) from decreasing to increasing, as the $p(CO_2)$ values increased. Nevertheless, the magnitude of the variation in E_a values in the initial part of the reaction was observed to be less than 10% with respect to the constant E_a value observed through for the main part of the reaction. Therefore, further kinetic analysis employing the master plot method was attempted using the average E_a value in

the α range of $0.1 \leq \alpha \leq 0.9$ listed in Table S1 (Figure 7c). The shapes of the normalized master plots of $(d\alpha/d\theta)_\alpha/(d\alpha/d\theta)_{0.5}$ versus α varied systematically vary with the $p(CO_2)$ values; in particular, the α value at the maximum reaction rate decreased as the $p(CO_2)$ value increased. Each master plot at a specific $p(CO_2)$ value was fitted by empirical kinetic models of SB(m, n, p) (eq 7) and Johnson-Mehl-Avrami, JMA(m) (eq 8).[92-95]

$$JMA(m): f(\alpha) = m(1-\alpha)[-\ln(1-\alpha)]^{1-1/m} \tag{8}$$

The results of model fittings are also listed in Table S1. Superficially, both empirical kinetic models exhibited a statistically significant fit to the experimental master plots, which empirically characterized the variation of the overall rate behavior with the $p(CO_2)$ values. Although JMA(m) was originally derived by considering the physicogeometrical features of the bulk nucleation and growth processes,[92-95] the optimized kinetic exponent m cannot have the physicochemical meanings in the present application to the thermal decomposition of $ZnCO_3$, as previously discussed for SB(m, n, p). However, the optimized kinetic exponents in SB(m, n, p) and JMA(m) provide an index to compare the apparent changes in the overall rate behaviors with atmospheric $p(CO_2)$ value. Using SB(m, n, p), the variation in the rate behavior was detected by the variations in the kinetic exponents characterized by the increases in n and p values and decrease in m value as the $p(CO_2)$ value increased. By contrast, a systematic decrease in m value as the $p(CO_2)$ values increased was evident using JMA(m). In both curve fitting results, the calculated A value increased with the $p(CO_2)$ value, exhibiting evidence of a mutual dependence between E_a and A values, known as the kinetic compensation effect (KCE).[96-102]
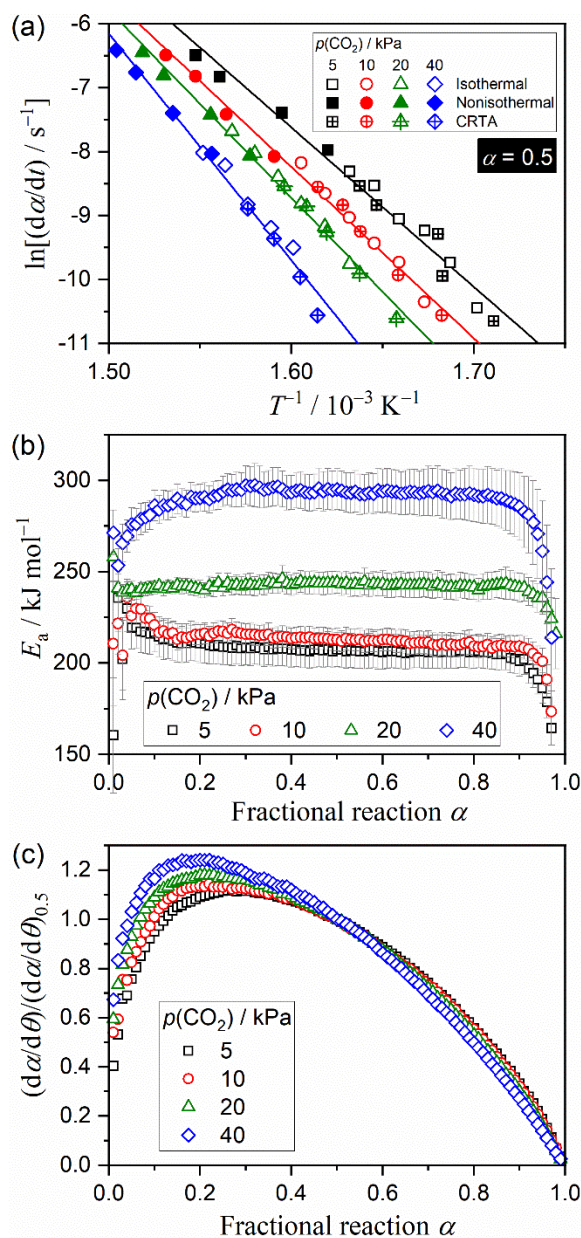
Figure 7. Results of the isoconversional kinetic analysis for the thermal decomposition of the $ZnCO_3$ sample under the individual conditions in a flow of N_2–CO_2 mixed gas with various $p(CO_2)$ values: (a) Friedman plots at $\alpha = 0.5$, (b) E_a values at various α values, and (c) experimental master plots of $(d\alpha/d\theta)/(d\alpha/d\theta)_{0.5}$ versus α.

As indicated by the evidence described above, performing the formal kinetic analysis of the thermal decomposition of $ZnCO_3$ in N_2-CO_2 atmospheres without considering the effect of $p(CO_2)$ results in different kinetic descriptions via different sets of kinetic triplet (i.e., E_a, A, and f(α)) among the reactions at different $p(CO_2)$ values. This generally observed situation when analyzing the thermal decomposition of inorganic solids should be addressed performing the universal kinetic description across different partial pressures of product gas in the reaction atmosphere, as well as across different reaction temperatures. The attempt has a long history of deriving the efficient AF concerning the effect of partial pressure of product gas to be introduced into the kinetic equation.[2,4,5,9,11,17,30] However, no generally

applicable AF has been put forward. Recently, we attempted to derive the analytical form of an AF to describe universally the kinetic behavior of the thermal decomposition of solids over different temperatures and partial pressures of product gas conditions, as exemplified by the studies performed on the thermal decomposition of divalent metal hydroxides[20-22] and the thermal dehydration of crystalline hydrates,[23] which were conducted taking into account the effect of atmospheric water vapor. The similar physicochemical approach was examined in the present study for revealing the effect that $p(CO_2)$ had on the kinetics of the thermal decomposition of as-prepared $ZnCO_3$. Based on the classical interfacial reaction theory,[55,103-108] the reaction scheme at the reaction interface was assumed to consist of the consecutive and concurrent occurrence of a series of elementary steps, including (1) creation of interstitial CO_2 defects at the internal interface, (2) diffusion of the interstitial CO_2 defects from the internal to the external interface, (3) consumption of the interstitial CO_2 defects at the external interface, (4) desorption of CO_2 molecules present on the external interface, and (5) consumption of Zn and O defects and formation of the ZnO building unit on the internal interface (see the scheme in Figure S25). The overall kinetics of the interfacial reaction is formulated based on the simple rate-limiting step and steady-state assumptions at a constant temperature, as listed in Table 1. In this approach, one elementary step is selected as the rate-limiting step, whereas all other elementary steps are assumed to be in equilibrium conditions, with each of these equilibria characterized by its own equilibrium constant (K_i). Notably, the product of all equilibrium constants is correlated to $P_{eq}(T)$ (atm) according to eq 9

$$K = K_1 K_2 K_3 K_4 K_5^{1/n} = \exp\left(-\frac{\Delta_r G^\circ}{RT}\right) = P_{eq}(T) \tag{9}$$

where $\Delta_r G^\circ$ is the Gibbs energy of the reaction. The kinetic expressions are classified into two forms.

$$v = k'\left(1 - \frac{p(CO_2)}{P^\circ P_{eq}(T)}\right) \tag{10}$$

$$v = k''\left(\frac{P^\circ}{p(CO_2)}\right)^n \left[1 - \left(\frac{p(CO_2)}{P^\circ P_{eq}(T)}\right)^n\right] \tag{11}$$

Equation 10 is derived for the cases whereby the elementary steps (1), (2), (3), or (4) were assumed to be rate-limiting, restricted by which $K_4 \gg p(CO_2)/P^\circ$ in the elementary step (3) and $K_1 K_2 K_4 \ll 1$ or $K_1 K_2 K_4 \gg 1$ in the elementary step of (4). The same kinetic equation expressing the effect of $p(CO_2)$ with eq 10 has been derived for the diffusional removal of CO_2 molecules through solid product layer.[5] The rate expression for the elementary steps (3) and (5) is generalized by eq 11, restricted by $K_4 \ll p(CO_2)/P^\circ$. Equations 10 and 11 have comparable forms to their counterparts derived for the thermal decomposition of metal hydroxides and the thermal dehydration of inorganic hydrates by taking into account the effect of water vapor pressure.[20-23] Consequently, an analytical form of the AF, $h(p(CO_2), P_{eq}(T))$, which accounts for both cases of eqs 10 and 11, is derived.

$$h\left(p(CO_2), P_{eq}(T)\right) = \left[\frac{P°}{p(CO_2)}\right]^a \left[1 - \left(\frac{p(CO_2)}{P°P_{eq}(T)}\right)^b\right] \tag{12}$$

where exponents a and b are constants that illustrate the types of the effect of $p(CO_2)$ characterized by the contributions of the first and second parts of the AF, i.e., $(P°/p(CO_2))^a$ and $[1 - (p(CO_2)/P°P^{eq}(T))^b]$. Notably, the AF presented in eq 12 is equivariant to the conventional AF when $(a, b) = (0, 1)$ (eq 2), which is the second part of the AF in eq 12. However, the contribution of the second part of the AF depends on the value of the expression $(p(CO_2)/P°P_{eq}(T))$ for the actual reaction. The $P_{eq}(T)$ values for the thermal decomposition of $ZnCO_3$ are reported in Figure S26, which were calculated using a thermodynamic database (MALT2, Kagaku Gijutsu-Sha).[109,110] The calculated $P_{eq}(T)$ values were larger than the experimentally applied $(p(CO_2)/P°)$ values (0.05-0.40 atm) by approximately 4 orders of magnitude in the actual reaction temperature range (580-690 K) of the thermal decomposition of the $ZnCO_3$ sample, indicating that the second part of the AF provides only a limited contribution to the correction of the experimental kinetic data by considering the influence of atmospheric $p(CO_2)$.

Table 1. Elementary steps of interfacial reaction expressed using Kröger's notation,[111] equilibrium constant for each elementary step, and kinetic equation for the process controlled by the selected elementary step

Elementary step i	Reaction	Equilibrium constant, K_i	Overall rate v for the process controlled by the elementary step i
(1) Creation of the interstitial CO_2 defect at the internal interface	$(CO_{3CO3})_{ZnCO3} \rightleftarrows (O_{CO3})_{ZnCO3} + (CO_{2,i,int})_{ZnO}$	$K_1 = [O_{CO_3}][CO_{2,\,i,\,int}]$	$v_1 = k_1\left(1 - \dfrac{p(CO_2)}{P^\circ P_{eq}(T)}\right)$
(2) Diffusion of the interstitial CO_2 defect from the internal to the external interface	$CO_{2,i,int} \rightleftarrows CO_{2,i,ext}$	$K_2 = \dfrac{[CO_{2,\,i,\,ext}]}{[CO_{2,\,i,\,int}]} = 1$	$v_2 = \dfrac{D_{CO_{2,i}}}{l_0} K_1 K_5 \left[1 - \left(\dfrac{p(CO_2)}{P^\circ P_{eq}(T)}\right)\right]$
(3) Consumption of the interstitial defect at the external interface	$CO_{2,i,ext} + (s) \rightleftarrows CO_2 - (s)$	$K_3 = \dfrac{[CO_2 - (s)]}{[(s)][CO_{2,\,i,\,int}]}$	$v_3 = k_3 \dfrac{K_1 K_4 K_5}{K_4 + p(CO_2)/P^\circ}\left(1 - \dfrac{p(CO_2)}{P^\circ P_{eq}(T)}\right)$
(4) Desorption of CO_2 molecule	$CO_2 - (s) \rightleftarrows CO_2(g) + (s)$	$K_4 = \dfrac{[(s)]p(CO_2)}{[CO_2 - (s)]}$	$v_4 = k_4 \dfrac{K_1 K_3 K_5}{1 + K_1 K_3 K_5}\left(1 - \dfrac{p(CO_2)}{P^\circ P_{eq}(T)}\right)$
(5) Consumption of the defect and formation of the ZnO building unit at the internal interface	$n(Zn_{Zn} + O_{CO3})_{ZnCO3} \rightleftarrows n(Zn_{Zn} + O_O)_{ZnO}$	$K_5 = \dfrac{[O_O]}{[O_{CO_3}]}$	$v_5 = k_5 \left(\dfrac{K_1 K_3 K_4 P^\circ}{p(CO_2)}\right)^n \left(1 - \left(\dfrac{p(CO_2)}{P^\circ P_{eq}(T)}\right)^n\right)$

By taking the logarithms of eq 1, we obtain eq 13

$$\ln\left[\frac{\left(\frac{d\alpha}{dt}\right)}{h\left(p(CO_2), P_{eq}(T)\right)}\right] = \ln[Af(\alpha)] - \frac{E_a}{RT} \tag{13}$$

When the AF in eq 12 is introduced into eq 13, a linear relation between the left-hand side of eq 13 and reciprocal temperature is expected for all data points at a given α value recorded under different heating and $p(CO_2)$ conditions through optimizing the most appropriate exponents (a, b) (modified Friedman plot).[20-23] Figure 8 summarizes the results of the modified isoconversional analysis based on eq 13 accompanied by eq 12. At individual α values, all of the data points aligned on a regression line with statistically significant correlations (Figures 8a and S27), demonstrating the universal isoconversional relation under different heating and $p(CO_2)$ conditions. The optimized exponents (a, b) were observed to remain approximately constant through the main part of the reaction ($0.1 \leq \alpha \leq 0.9$) (Figure 8b), accompanied by the average values (0.95 ± 0.01, 0.55 ± 0.03), respectively. With respect to the b value, it displayed a decreasing trend in the early stages of the reaction ($\alpha < 0.1$) and an increasing trend in its final stage ($\alpha > 0.9$); notably, in the final stage of the reaction, the increase in b value was accompanied by a decrease in the a value. The E_a values calculated from the slopes of the modified Friedman plots at various α values (Figure 8b) were indicative of a similar variation trend with that observed for the reaction in a flow of dry N_2 gas (Figure 4); in particular, an initial decrease was observed from approximately 250 to 235 kJ mol^{-1} ($\alpha \leq 0.1$); subsequently, E_a displayed an approximately constant value of 234.5 ± 4.6 kJ mol^{-1} in the main reaction stage ($0.1 \leq \alpha \leq 0.9$), followed by a rapid drop in E_a value to approximately 80 kJ mol^{-1} in the final stage ($\alpha > 0.9$). The mentioned drop in E_a value is expected to correspond to the reaction tail, which is controlled by the diffusional removal of the gaseous product.
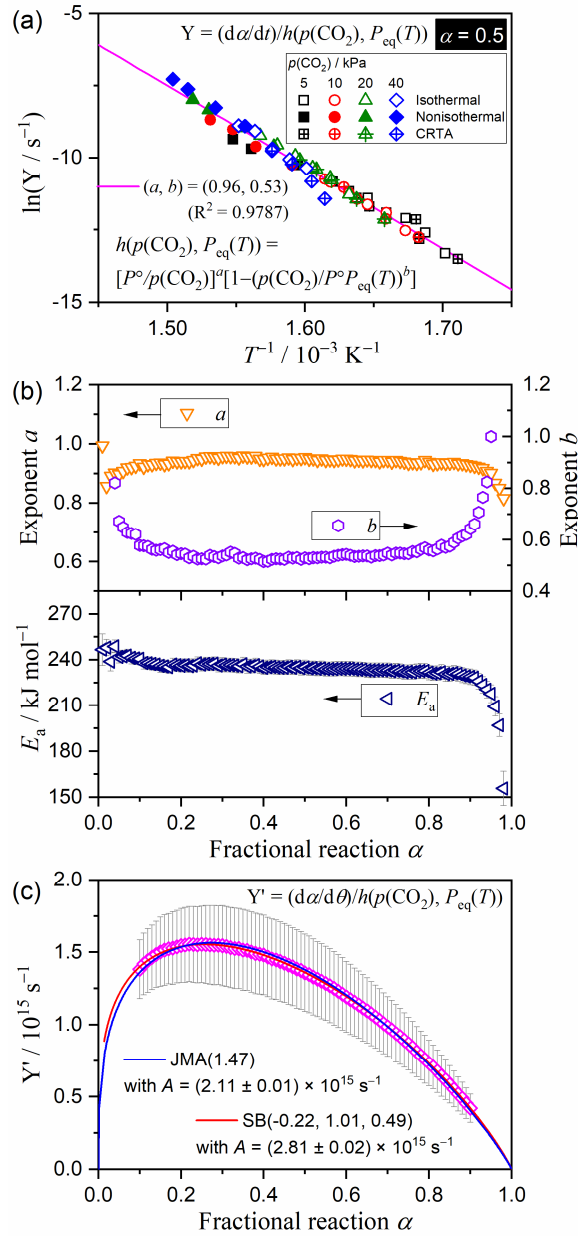
Figure 8. Results of the Friedman plot, modified by introducing the AF in eq. (12), for the thermal decomposition of the $ZnCO_3$ sample in a flow N_2–CO_2 mixed gas with various $p(CO_2)$ values: (a) modified Friedman plots at $\alpha = 0.5$, (b) exponents (a, b) in the AF at various α, (c) E_a values at various α, and (d) experimental master plot and the fitting curves using SB(m, n, p) and JMA(m).

Based on the universal kinetic equation (eq 1), the experimental master plot was also modified by the introduction of h($p(CO_2)$, $P_{eq}(T)$), as $(d\alpha/d\theta)$/h($p(CO_2)$, $P_{eq}(T)$) versus α.

$$\frac{\left(\frac{d\alpha}{d\theta}\right)}{h(p(CO_2), P_{eq}(T))} = \frac{\frac{d\alpha}{dt}\exp\left(\frac{E_a}{RT}\right)}{h(p(CO_2), P_{eq}(T))} = Af(\alpha) \tag{14}$$

By assuming a single-step reaction characterized by an E_a value of 234.5 kJ mol^{-1} and using the AF in eq 12, with (a, b) = (0.95, 0.55), the modified experimental master plot was drawn by calculating the

(dα/dθ)/h(p(CO_2), P_{eq}(T)) values at various values for α (Figure 8c). The universal master plot also indicates the maximum rate midway through the reaction as in the conventional master plot drawn for the reactions under respective p(CO_2) conditions (Figure 7c), indicating satisfactory fittings using the empirical kinetic models of SB(-0.22 ± 0.07, 1.01 ± 0.03, 0.49 ± 0.07), with A = (2.81 ± 0.02) × 10^{15} s^{-1}, and JMA(1.47 ± 0.01), with A = (2.11 ± 0.01) × 10^{15} s^{-1}. Despite the statistically significant fitting of the universal master plot with SB(m, n, p) and JMA(m), the physicogeometrical mechanism of the thermal decomposition of the $ZnCO_3$ sample was apparently characterized by the contracting-geometry-type reaction induced by the SR. The SEM images of the partially decomposed samples to different α values, obtained by performing a nonisothermal heating at a β of 5 K min^{-1} to different final temperatures in a flow of N_2-CO_2 mixed gas (p(CO_2) = 40 kPa), exhibited characteristics that suggested that practically the same morphological changes had occurred with respect to those taking place in the analogous process carried out in a flow of dry N_2 gas; in fact, the original polyhedral particle shape was maintained during the reaction (Figure S28). For such a reaction, the initial acceleration in the universal master plot (Figure 8c) is interpreted as being caused by the contribution of the SR to the overall kinetics. Thus, use of the Mampel's model[112] for the consecutive SR and subsequent phase boundary-controlled reaction (PBR) under isothermal conditions is a possible approach to modeling the kinetics of such reactions.[113] The differential kinetic equations for the SR-PBR(n) models derived by assuming a first-order SR and an n-dimensional PBR[114] are listed in Table S2. The practical kinetic analysis based on the SR-PBR(n) models is the nonlinear least-squares analysis to fit each isothermal kinetic curve with the calculated curve based on the kinetic equations listed in Table S2 through optimization of the respective rate constants for the SR and PBR(n) steps (i.e., k_{SR} and k_{PBR}(n)). The calculation procedure is detailed in Section S5.5 in the Supporting Information. Figure 9 shows the typical fitting results of an isothermal kinetic curve using the SR-PBR(n) models. Comparing the statistical significances of the fitting using the SR-PBR(n) models with different n values, the model assumed threedimensional PBR (SR-PBR(3)) was selected as the most appropriate model for describing the overall kinetics, irrespective of the measurement temperature and p(CO_2) value. The interface shrinkage dimension expected by the mathematical model fitting is reasonable, when considering the polyhedral shape of the sample particles. Table S3 lists the values for k_{SR} and k_{PBR}(3) determined for the individual kinetic curves recorded at different temperature and p(CO_2) values. The conventional Arrhenius plots applied to the k_{SR} and k_{PBR}(3) values were characterized by different linear correlations for the data at different p(CO_2) values in both the SR and PBR(3) steps, in which the Arrhenius plots displayed approximately parallel shifts as a result of changes in the p(CO_2) values (Figure S29). The apparent Arrhenius parameters for the SR and PBR(3) steps at different p(CO_2) values are listed in Table S4.
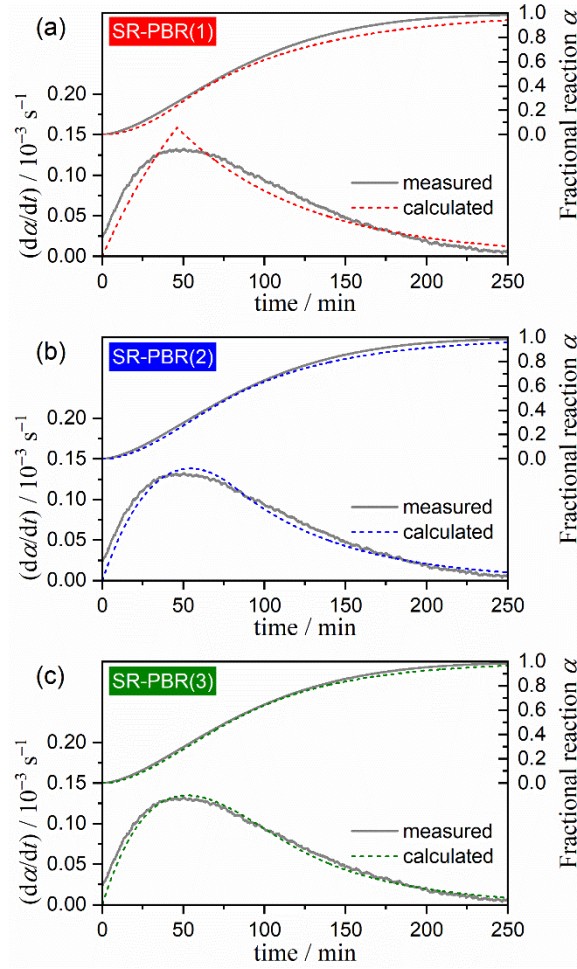
Figure 9. Typical fittings of the isothermal kinetic curve ($T = 613$ K and $p(CO_2) = 10.0$ kPa) using the SR–PBR(n) models.

To obtain the universal kinetic description under different temperature and p(CO_2) conditions, the AF for describing the effect of p(CO_2) was introduced in the Arrhenius equation

$$k = A\exp\left(-\frac{E_a}{RT}\right) h\left(p(CO_2), P_{eq}(T)\right) \tag{15}$$

Figure 10 shows the Arrhenius plots modified by introducing the AF in eq 12 for the SR and PBR(3) steps. Through optimization of the exponents (a, b) in eq 12, all data points referring to different temperatures and p(CO_2) values aligned on a single straight line, with statistically significant correlations determined to exist in both reaction steps. The results evidence the universal kinetic description over different temperatures and p(CO_2) values in each reaction step. The kinetic parameters determined by the modified Arrhenius plots are listed in Table 2. Comparing the values of the exponents (a, b) in eq 12 between the SR and PBR(3) steps, an apparent decrease in the a value became obvious as the reaction step advanced from SR to PBR(3); by contrast, the b value appeared to be practically invariant. The variation of the a value is indicative of the more significant effect of p(CO_2) value on the SR than that on PBR(3), which is reasonable, considering the direct interaction between the atmospheric

CO₂ and the surface of the reactant particles. The values of the Arrhenius parameters (E_a, ln A) also decreased as the reaction step advanced from SR to PBR(3). This trend is in agreement with the variation trend of the isoconversional E_a values determined by the modified Friedman plots (Figure 8b). Notably, the E_a value for the PBR(3) step is quite close to the average value of the isoconversional E_a through the main part of the reaction.
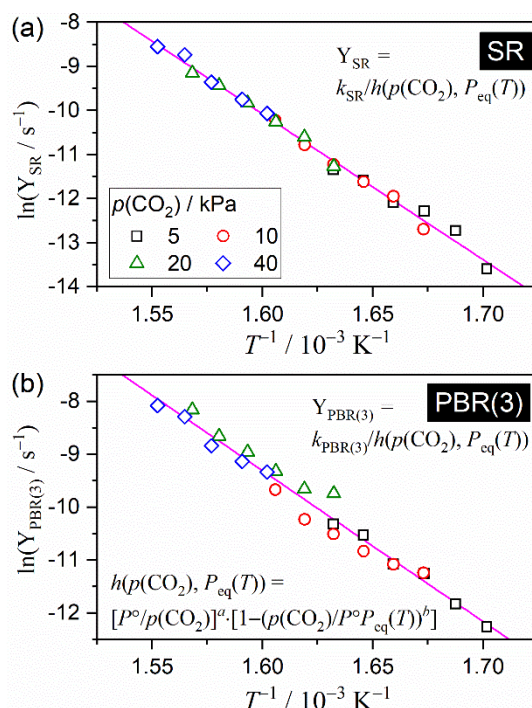
Figure 10. Arrhenius plots modified by introducing the AF in eq. (12): (a) SR and (b) PBR(3) steps.

Table 2. Kinetic parameters determined by the modified Arrhenius plots shown in Figure 15

Reaction step	Eq. (12)		E_a / kJ mol⁻¹	$\ln(A\ /\ \text{s}^{-1})$	$-\gamma$ [a]
	a	b			
SR	1.30	1.92	274.6 ± 5.4	42.8 ± 1.1	0.9959
PBR(3)	0.69	2.05	236.9 ± 8.6	36.3 ± 1.7	0.9867

[a] Correlation coefficient of the linear regression analysis.

3.5. Thermal Decomposition of ZnCO₃ in N₂-H₂O Atmosphere.

Figure 11 shows the TG-DTG curves for the thermal decomposition of the $ZnCO_3$ sample recorded at a fixed heating rate of 5 K min⁻¹ in a flow of N₂-H₂O mixed gases characterized by different $p(H_2O)$ values. In contrast with the effect of the $p(CO_2)$ value in the corresponding process carried out in a flow of N₂-CO₂ mixed gas, the TG- DTG curves significantly shifted to lower temperatures as the $p(H_2O)$ value increased (Figure 11a), although the shapes of TG and DTG curves practically did not change.

Figure 11. TG–DTG curves for the thermal decomposition of the $ZnCO_3$ sample ($m_0 = 4.983 \pm 0.034$ mg) recorded at a fixed β of 5 K min^{-1} in a flow of N_2–H_2O mixed gas with different $p(H_2O)$ values.
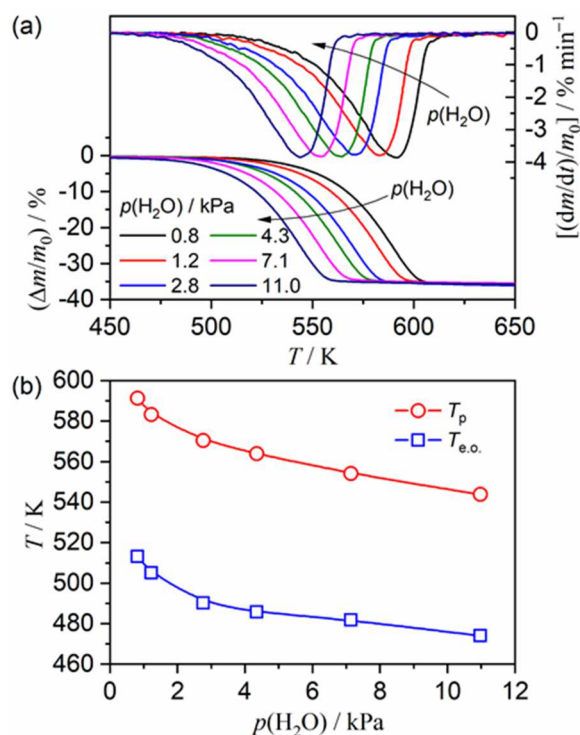
The parallel shift of the TG-DTG curves along the temperature axis is made evident by the practically constant temperature gap between the extrapolated onset (T_{eo}) and peak top (T_p) temperatures in the DTG curves measured at different p(H_2O) values (Figure 11b). Similar phenomena induced changes in atmospheric p(H2O) values have also been reported for the thermal decompositions of $CaCO_3$,[36-44] synthetic malachite,[31-34,63] and hydrozincite.[16,35,64] Since water molecules are neither reactants nor products of the thermal decomposition of $ZnCO_3$, a catalytic activity should be considered to explain the changes in the TG-DTG curves associated with changes in the p(H_2O) value. Notably, the features of changes in the particle morphologies and surface textures of the $ZnCO_3$ particles as the thermal decomposition of $ZnCO_3$ progressed in the presence of water vapor, as made evident by the SEM images shown in Figure S30, indicated no distinguishable differences from those for the reactions in a flow of dry N_2 and N_2-CO_2 mixed gases. The kinetic behavior of the thermal decomposition at a fixed p(H_2O) value of 9.56 kPa was analyzed using the TG-DTG curves recorded under isothermal, linear nonisothermal, and CRTA conditions (Figure 12). The kinetic curves converted from these TG-DTG curves are reported in Figure S31 as three-dimensional plots in the time-T-α and time-T-dα/dt coordinates.
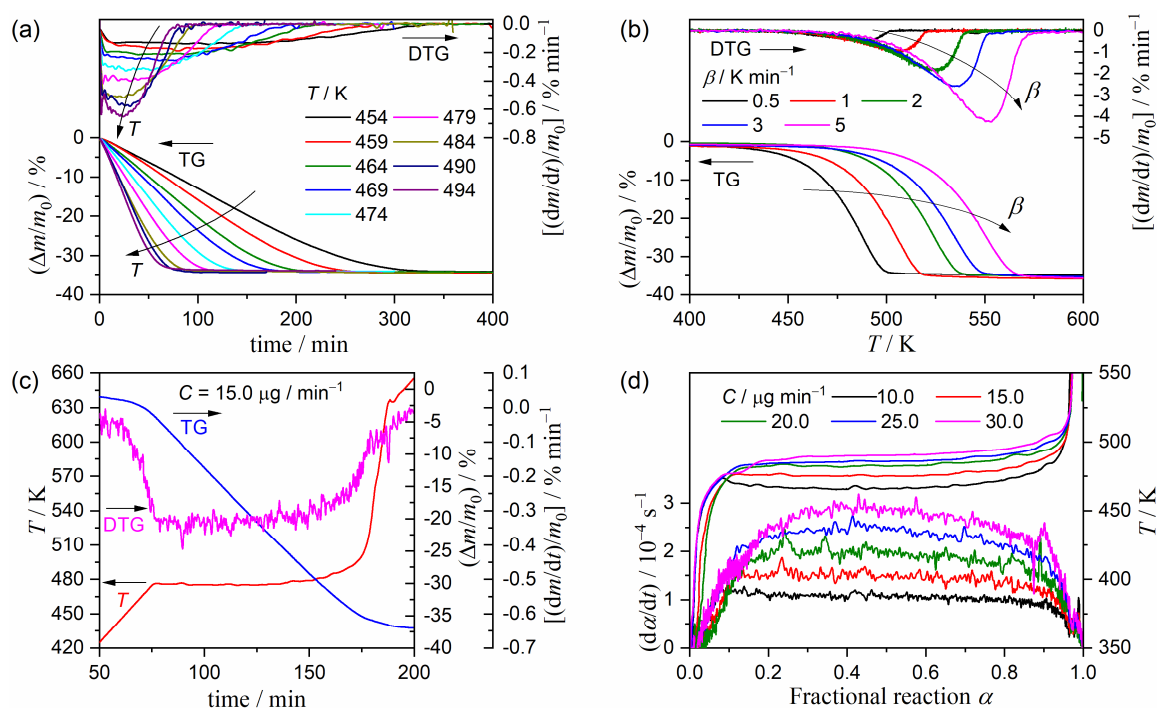
Figure 12. TG–DTG curves for the thermal decomposition of the $ZnCO_3$ sample recorded in a flow of N_2–H_2O mixed gas with $p(H_2O) = 9.56$ kPa under various heating conditions: (a) isothermal conditions, (b) nonisothermal conditions, (c) typical CRTA record, and (d) temperature profiles and DTG curves under CRTA conditions.

Initially, the kinetic curves at a fixed $p(H_2O)$ value of 9.56 kPa were analyzed simultaneously through the conventional isoconversional kinetic approach, without considering the effect of $p(H_2O)$ (Figure 13). The Friedman plots exhibited statistically significant linear correlations, irrespective of the α values (Figure 13a); moreover, the slopes of the plots remained approximately constant as the α value varied. Therefore, approximately constant E_a values were obtained during the course of the reaction, except at the very beginning and end of the thermal decomposition of $ZnCO_3$ (Figure 13b). The average E_a value through the main part of the reaction $(0.1 \leq \alpha \leq 0.9)$ was 75.8 ± 1.1 kJ mol^{-1}. The experimental master plots of $(d\alpha/d\theta)$ versus α exhibited the maximum rate midway through the reaction (Figure 13b), an observation well fitted by SB(-2.59, 1.53, 2.76) with $A = (4.47 \pm 0.05) \times 10^4$ s^{-1}. The estimated Arrhenius parameters (E_a, A) were much smaller than those determined for the reaction conducted in a flow of dry N_2 gas. However, the experimental master plots for the reaction conducted in a flow of dry N_2 and N_2-H_2O mixed gas characterized by a $p(H_2O)$ value of 9.56 kPa were practically equal in shape (Figure S32), as expected from the parallel shift of the TG-DTG curves along the temperature axis as a result of the change in the $p(H_2O)$ value.
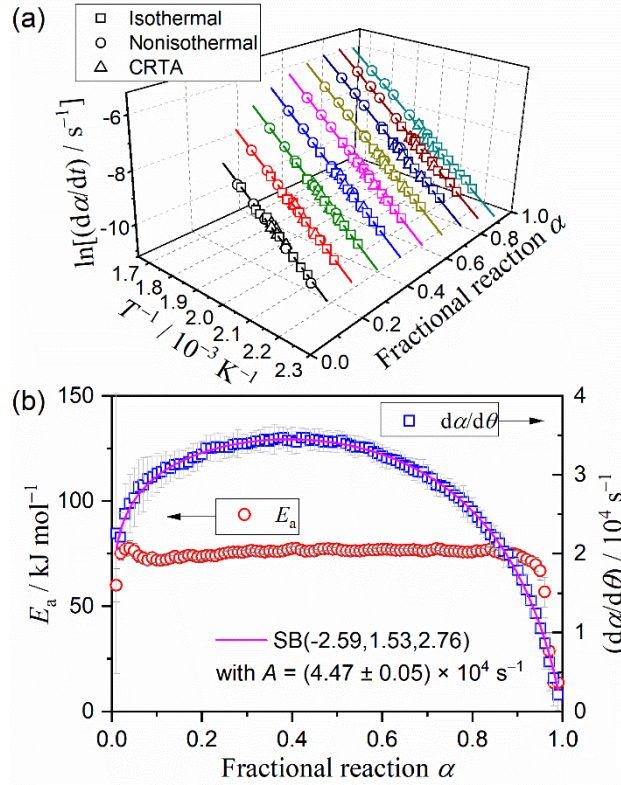
Figure 13. Results of the conventional kinetic approach to the thermal decomposition of the $ZnCO_3$ sample in a flow of N_2–H_2O mixed gas with a fixed $p(H_2O)$ of 9.56 kPa: (a) Friedman plots at various α, (b) E_a values at various α, (c) experimental master plots of $(d\alpha/d\theta)$ versus α.

Similar to the case of the effect of $p(CO_2)$ on the kinetics of the thermal decomposition, introduction of an AF that accounts for the effect of atmospheric water vapor, that is $h(p(H_2O))$, in the fundamental kinetic equation may be a practical solution for explaining the effect of $p(H_2O)$ on the kinetics of the thermal decomposition

$$\frac{d\alpha}{dt} = A\exp\left(-\frac{E_a}{RT}\right)f(\alpha)h\big(p(H_2O)\big) \tag{16}$$

By taking logarithms of eq. (16) after rearrangement, we obtain eq. (17) for the kinetic analysis of individual kinetic curves (differential single run method):[115]

$$\ln\left[\frac{\left(\frac{d\alpha}{dt}\right)}{f(\alpha)\cdot h\big(p(H_2O)\big)}\right] = \ln A - \frac{E_a}{RT} \tag{17}$$

Assuming an invariant kinetic model function irrespective of $p(H_2O)$ values, i.e., SB(-2.59, 1.53, 2.76), the kinetic curves converted from the TG-DTG curves recorded at a fixed β value of 5 K min^{-1} under various $p(H_2O)$ conditions and at various β or C values under a fixed $p(H_2O)$ value of 9.56 kPa were analyzed by the differential single-run method based on eq 17 (Figure 14). When the effect of $p(H_2O)$

was ignored by imposing a value of 1 for h(p(H$_2$O)) in eq 17, plots of the logarithmic term in the left-hand side of eq 17 versus the reciprocal temperature exhibited statistically significant linear correlations for the individual reactions under different p(H$_2$O) conditions (Figure 14a). These plots were observed to shift in parallel as the p(H$_2$O) value varied, although those for the reactions conducted at a fixed value for the p(H$_2$O) were observed to form a single straight line for different heating conditions. The E_a and A values determined by the single-run method without considering the effect of p(H$_2$O) were observed to undergo a systematic decrease as the p(H$_2$O) value increased (Table S5). In addition, a statistically significant linear correlation between the apparent E_a and $\ln A$ values (i.e., $\ln A = a + bE_a$), was observed to exist, as in the manner of the KCE (Figure S33).[96-102] This implies that conventional kinetic approaches whereby the effect of p(H$_2$O) is not considered do not provide a universal kinetic description of the thermal decomposition of ZnCO$_3$ under various p(H$_2$O) values.
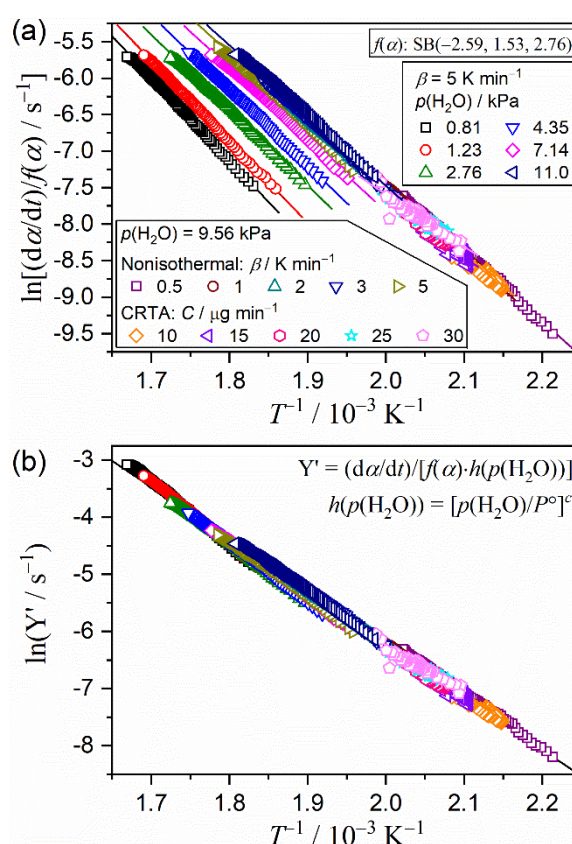
Figure 14. Kinetic plots based on eq. (16) for the thermal decomposition of the ZnCO$_3$ sample under various heating and p(H$_2$O) conditions: (a) differential single run method applied to the individual kinetic curves with an assumption of $h(p$(H$_2$O)$) = 1$ and (b) universal kinetic plot for all kinetic curves drawn by introducing $h(p$(H$_2$O)$)$ presented in eq. (18).

In view of the chemical reaction process, the catalytic action of atmospheric water vapor is explained by the contribution of water molecules to the elementary steps of surface and interfacial reactions. Some simple models of the consecutive elementary steps that take into account the contribution of water

molecules have been proposed to explain its catalytic action observed in the thermal decomposition of $CaCO_3$.[43,44] In those models, formation of hydrogen carbonate HCO_3^- species as a result of the reaction between CO_3^{2-} ions on the surface of $CaCO_3$ and water molecules adsorbed at Ca-bridge sites of $CaCO_3$ and the subsequent dissociation of HCO_3^- into CO_2 and OH^- were considered as the possible reaction pathway catalyzed by atmospheric water vapor. On the basis of the physicogeometrical reaction scheme, an enhancement in the rate of crystal growth of the solid product, ZnO, affected by atmospheric water vapor may be an alternative cause of the apparent catalytic behavior of water molecules in the thermal decomposition of $ZnCO_3$. Notably, this phenomenon has been observed for different metal oxides.[57-62] A slight but detectable increase in the growth rate of ZnO crystallites triggered by atmospheric water vapor was also observed in this study (Figure S11). The crystal growth of ZnO in the surface product layer generates interstices, which may facilitate the diffusional removal of CO_2 from the reaction interface. In both models introduced to explain the catalytic effect of atmospheric water vapor, the adsorption of water molecules on the reactant or product solid is the key process. Considering the adsorption equilibrium of water molecules on solid surfaces, the amount of adsorbed water molecules at a specific temperature depends on the $p(H_2O)$ value. To evaluate the influence that water vapor has on the kinetics of thermal decomposition of $ZnCO_3$, the AF can have the following form[19,38]

$$h\big(p(H_2O)\big) = \left(\frac{p(H_2O)}{P^\circ}\right)^c \tag{18}$$

where c is a constant accounting for the contribution of $p(H_2O)$ to the overall reaction rate. By introducing the analytical form of $h(p(H_2O))$ in eq 17, all kinetic curves obtained under different heating and $p(H_2O)$ conditions were universally analyzed, a process that enabled us to determine the value of exponent c in eq 18 affording the best linear correlation (Figure 14b). In particular, when c = 0.546, all data points of the kinetic curves were observed to align on a single straight line representing the universal kinetic relationship over different heating and $p(H_2O)$ conditions. The kinetic parameters determined by the universal kinetic analysis are listed in Table 3.

Table 4. Kinetic results of the universal kinetic approach for the thermal decomposition of the $ZnCO_3$ sample under various heating and $p(H_2O)$ conditions

Universal method	c	E_a / kJ mol^{-1}	A / s^{-1}	SB(m, n, p)			$R^{2,\,a}$
				m	n	p	
Single run	0.546	76.4 ± 0.2	(1.9 ± 0.1) × 10^5	−2.59	1.53	2.76	0.9973
Isoconversional	0.524 ± 0.03	74.9 ± 0.6	(1.4 ± 0.1) × 10^5	−2.13 ± 0.13	1.38 ± 0.05	2.35 ± 0.12	0.9988

[a]Determination coefficients of the linear and nonlinear least squares analyses for the universal kinetic plot in model-fitting approach and the fitting of the experimental master plots using SB(m, n, p) in isoconversional approach, respectively.

A rearrangement of eq 17 provides a kinetic equation affording the universal kinetic analysis of the isoconversional kinetic relationship for different heating and $p(H_2O)$ conditions

$$\ln\left[\frac{\left(\frac{d\alpha}{dt}\right)}{h(p(H_2O))}\right] = \ln[Af(\alpha)] - \frac{E_a}{RT} \tag{19}$$

Figure 15 summarizes the results of the isoconversional kinetic analysis based on eq 19 with $h(p(H_2O))$ in eq 18. Irrespective of α, the modified Friedman plots exhibited statistically significant linear correlations for all kinetic data under different heating and $p(H_2O)$ conditions, when the optimized c value was utilized in each plot (Figure 15a). Notably, the optimized values for c were approximately constant through the main part of the reaction ($0.1 \leq \alpha \leq 0.9$), with an average value of $c = 0.524 \pm 0.03$ (Figure 15b), which closely matches the value determined through the kinetic plot obtained implementing the differential single-run method (Figure 14b). The E_a values were also observed to remain constant in a wide range of α values (Figure 15b), with the average value for this parameter determined to be $E_a = 74.9 \pm 0.6$ kJ mol^{-1}. The experimental master plot based on eq 16 can be presented as follows (eq 20)

$$\frac{\left(\frac{d\alpha}{d\theta}\right)}{h(p(H_2O))} = \frac{\frac{d\alpha}{dt}\exp\left(\frac{E_a}{RT}\right)}{h(p(H_2O))} = Af(\alpha) \tag{20}$$

The universal experimental master plot drawn for the reactions under various heating and $p(H_2O)$ conditions using the average values of c and E_a in the $0.1 \leq \alpha \leq 0.9$ range (Figure 15c) displayed a shape comparable with those drawn previously for the reactions conducted in a flow of dry N_2 and at $p(H_2O)$ = 9.56 kPa (Figure S32). Table 3 also lists the kinetic parameters determined by the isoconversional kinetic approach considered the catalytic action of atmospheric water vapor. The fact that implementation of the universal single-run and isoconversional methods afforded comparable kinetic results supports the idea that a successful kinetic characterization of the thermal decomposition of $ZnCO_3$ under various heating and $p(H_2O)$ conditions has been achieved.
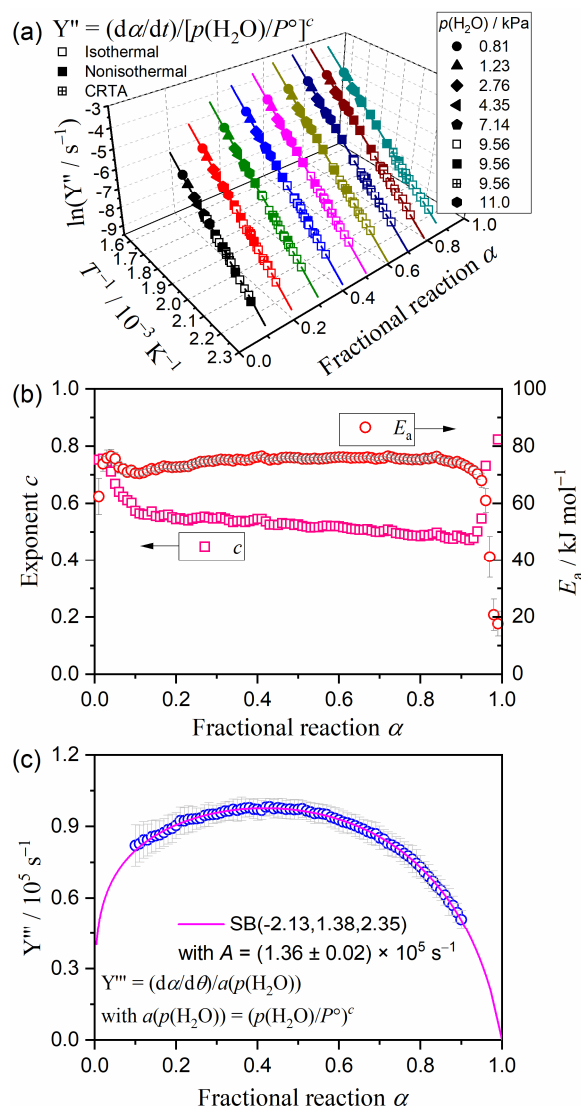
Figure 15. Kinetic results obtained by the isoconversional kinetic analysis modified by introducing $h(p(H_2O))$ in eq. (18) for the thermal decomposition of the $ZnCO_3$ sample under various heating and $p(H_2O)$ conditions: (a) modified Friedman plots at different α values, (b) optimized exponent c in eq, (18) at different α values, (c) E_a values at different α values, and (d) universal master plot and fit curve using SB(m, n, p).

3.6. Physicogeometrical Kinetic Interpretations.

To interpret the effect that atmospheric CO_2 and water vapor had on the kinetics of the thermal decomposition of as-prepared $ZnCO_3$ samples, the thermal decomposition taking place in a flow of dry N_2 gas is to be a reference process. The reaction kinetics can be understood based on the physicogeometrical reaction scheme and the consecutive physicogeometrical steps of the surface nucleation and interfacial reaction. The reaction conducted in a flow of dry N_2 was characterized by an approximately constant value for E_a (104.7 ± 2.9 kJ mol^{-1}) in the $0.1 \leq \alpha \leq 0.9$ range, although E_a was observed to initially decrease from 140 to 105 kJ mol^{-1} ($\alpha \leq 0.1$). The E_a variation at the beginning of the thermal decomposition was assumed to be the contribution of the SR process, whereas the

subsequent phase of the reaction was described as the result of the contracting geometry of the reaction interface. Based on the classical nucleation theory, surface nucleation is understood to comprise several elementary steps: (i) creation of interstitial CO_2 defects, (ii) desorption of CO_2 molecules, and (iii) formation of the ZnO building unit. Therefore, the reaction initiation temperature may vary depending on the atmospheric conditions, given that specific gases present in the atmosphere contribute to the elementary steps of surface nucleation. The established reaction occurs at the $ZnO/ZnCO_3$ interface, which is characterized by the presence of zones of locally enhanced reactivity (Figure S25). In addition to the interfacial process, the crystal growth of ZnO in the surface product layer and the diffusion-driven removal of thus-produced CO_2 through the surface product layer influence on the overall kinetics of the established reaction. Notably, the process of interface advancement also comprises several elementary steps, which are listed in Table 1. Each elementary step is directly influenced by the presence of self-generated CO_2. The influence of the atmospheric conditions on the interfacial reaction is thus understood to be caused by the complex interactions of the effects on the specific component processes and steps. Evidence suggests that atmospheric CO_2 causes the overall reaction rate to decrease and the initiation temperature of the reaction to shift to higher values (Figure 5). The shapes of the mass-loss curves drawn for the reactions conducted in a flow of N_2-CO_2 mixed gases at a constant temperature exhibited a more obvious sigmoidal shape than their counterparts obtained for the reactions conducted in a flow of dry N_2 gas (Figure S16), indicating the physicogeometrical consecutive SR-PBR as a possible model for describing the kinetic behavior. This observation was also supported by the experimental master plots drawn based on the conventional isoconversional analysis, which exhibited the maximum reaction rate midway through the overall reaction (Figure 7c). An increase in atmospheric $p(CO_2)$ value would directly affect the elementary steps of surface nucleation, causing the temperature of the reaction initiation to shift to higher values. At higher temperatures, in contrast, the rate of the evolution of CO_2 produced by the reaction increases. At the same time, atmospheric CO_2 retards the growth of ZnO crystals (Figure S11), causing the formation of a more compact surface product layer. The increase in CO_2 evolution rate at the reaction interface and the enhanced difficulty of this molecule's diffusional removal result in an increase in the self-generated $p(CO_2)$ at the reaction interface. This increase in turn results in a retardation of the elementary steps of the interfacial reaction. A quantitative evaluation of the effect that atmospheric $p(CO_2)$ had on the overall kinetics was realized through the isoconversional analysis by introducing the AF in eq 12. The results thus obtained also indicated that kinetic modeling was possible based on the consecutive SR-PBR, in views of the variation in the universal E_a value as the reaction advanced and the specific shape of the universal master plot characterized by the maximum reaction rate midway through the overall reaction (Figure 8). The universal kinetic modeling of the SR-PBR(3) over different $p(CO_2)$ values afforded a quantitative characterization of the difference in the effects of $p(CO_2)$ on SR and PBR(3); evidence indicated the exponent a in eq 12 to be twice as large for SR than for PBR(3); additionally, the Arrhenius parameters were larger for SR than for PBR(3) (Table 2). These observations indicated that atmospheric $p(CO_2)$ had a more significant effect on SR than on

PBR(3), as a result of the direct exposure of the reactant surface to the reaction atmosphere. By contrast, atmospheric water vapor significantly accelerated the thermal decomposition of the $ZnCO_3$ sample, as evidenced by the systematic shift of the TG-DTG curves to lower temperature values in association with increasing $p(H_2O)$ values (Figure 11). Importantly, neither the presence of atmospheric water vapor nor increases in $p(H_2O)$ induced any changes in the shape of the TG-DTG curves and the geometrical mechanism of the thermal decomposition. In the presence of atmospheric water vapor, the positive evidence of the enhanced crystal growth of ZnO was observed (Figure S11). This phenomenon causes an increase in size of the interspace between the ZnO crystalline particles in the surface product layer, which would facilitate the diffusional removal of the gases evaluated by the thermal decomposition at the internal reaction interface. In view of the elementary steps of the thermal decomposition of $ZnCO_3$ at the atomic scale, the water molecule is expected to act as a catalyst promoting the dissociation of CO_3^{2-} via the generation of HCO_3^-. These expected phenomena lead the formal kinetic description by considering the catalytic effect of $p(H_2O)$ using the AF of $(p(H_2O)/P^\circ)^c$. The kinetic data recorded under different temperature and $p(H_2O)$ conditions are universally described with the exponent c in the AF of approximately 0.5 and a single set of the Arrhenius parameters (E_a, A) values of approximately 75 kJ mol^{-1} and $\sim 10^5$ s^{-1}, respectively. The universal kinetic descriptions of the thermal decomposition of the $ZnCO_3$ sample under conditions whereby either the $p(CO_2)$ or the $p(H_2O)$ value were made to vary characterized well the retardation and catalytic effects via the observed increase or decrease in the apparent Arrhenius parameters, respectively.

4. CONCLUSIONS

$ZnCO_3$ samples having the crystal structure of smithsonite were synthesized performing the same hydrothermal treatment of mixed precipitates composed of $ZnCO_3$ and $Zn_5(CO_3)_2(OH)_6$ in $NaHCO_3(aq)$ at 373 K a number of times in sequence. The thermal decomposition of $ZnCO_3$ proceeded with a smooth mass-loss accompanied by a DTA endothermic peak to produce ZnO, without any indication or positive evidence of the formation of crystalline intermediates. In a flow of dry N_2 gas, the kinetic description of the thermal decomposition of $ZnCO_3$ is characterized by $E_a = 104.7 \pm 2.9$ kJ mol^{-1} and $A = (8.56 \pm 0.09) \times 10^5$ s^{-1}. However, the decreasing trend in E_a value during the early stages of the reaction and the convex shape of the experimental master plot of $d\alpha/d\theta$ versus α indicate the possible contribution of SR to the overall contracting-geometry-type reaction. The specific characteristics of the kinetics are the retardation and catalytic effects that atmospheric CO_2 and H_2O have, respectively. The retardation effect of CO_2 on the thermal decomposition of metal carbonates is generally considered in relation to the reaction equilibrium. However, the thermal decomposition of $ZnCO_3$ occurs at temperatures that are much higher than the equilibrium temperature of the decomposition reaction $ZnCO_3(s) \rightarrow ZnO(s) + CO_2(g))$ at a given $p(CO_2)$ value, and at $p(CO_2)$ values that are much lower than the Peq value at a given temperature. Therefore, the $p(CO_2)$ term in the first part of eq 12 (i.e., $(P^\circ/p(CO_2))^a$), is the practical

form of the AF for describing the kinetic behavior of the reaction over different $p(CO_2)$ values. Introduction of the AF (eq 12) into the fundamental kinetic equation allows us to investigate the isoconversional kinetic relationship over different heating and $p(CO_2)$ conditions, as demonstrated by the universal Friedman plot based on eq 13 and the experimental master plot based on eq 14 (Figure 8). From the standpoint of a physicogeometrical reaction mechanism, the consecutive SR-PBR features become more evident for the reaction as the $p(CO_2)$ value increased. The kinetic behaviors of the SR and PBR under isothermal conditions can also be universally described with the aid of the AF (eq 12), so as to provide the kinetic parameters (a, b, E_a, and ln A) for the respective physicogeometrical reaction steps (Table 2). The thermal decomposition of $ZnCO_3$ was observed to be significantly accelerated by the presence of atmospheric water vapor; in fact, the decomposition temperature decreased as the $p(H_2O)$ value increased. However, the physicogeometrical reaction mechanism remained practically unchanged by the catalytic activity of atmospheric water vapor. The possible relevant catalytic mechanism may be related to the enhancement of the thermal decomposition of $ZnCO_3$ via the formation of HCO_3^- by the interaction of $ZnCO_3$ surfaces with adsorbed water molecules or the promotion of ZnO crystal growth by water molecules adsorbed onto the ZnO surfaces. An alternative AF in the form of $(p(H_2O)/P°)^c$ can be derived considering the adsorption probability of water molecules for describing universally the thermal decomposition of $ZnCO_3$ over different heating and $p(H_2O)$ conditions. The practical applicability of the AF described by eq 18 is demonstrated by the universal single-run plot based on eq 17 (Figure 14) and isoconversional analysis based on eq 19 (Figure 15), whereby practically identical kinetic parameters were obtained, including the exponent c in the AF (Table 3). As demonstrated through the practical kinetic analysis for the thermal decomposition of $ZnCO_3$ under various atmospheric conditions, the introduction of an appropriate AF in the fundamental kinetic equation allows us to perform the universal kinetic analysis of complex reaction systems composed of solids and gases over different heating and atmospheric conditions, in view of the formal kinetic approach. This conclusion can also be extended to the universal physicogeometrical kinetic description, like that based on the SR-PBR model. The form of AF and the magnitude of the parameters in it can provide supplementary kinetic information on the thermal decomposition of solids, in addition to the conventional kinetic triplet (i.e., E_a, A, and f(α)). The types and intensity of the effects of different atmospheric gases on the kinetics of a reaction may be classified by investigating the most appropriate form of the AF and the actual values of the parameters in it, which is expected to be a provision for establishing the advanced theory of the kinetics of thermal decomposition of solids and solid-gas reactions.

ASSOCIATED CONTENT

Supporting Information: S1. Preparation and Characterization of the Precursor (Figures S1–S3), S2. Preparation and Characterization of the $ZnCO_3$ sample (Figures S4–S7), S3. Thermal behavior of

the $ZnCO_3$ sample (Figures S8–S13), S4. Thermal decomposition in dry N_2 atmosphere (Figures S14 and S15), S5. Thermal decomposition in N_2–CO_2 atmosphere (Figures S16–S29, Tables S1–S4), and S6. Thermal decomposition in N_2–H_2O atmosphere (Figures S30–S33).

AUTHOR INFORMATION

Corresponding Author

Nobuyoshi Koga - Department of Science Education, Graduate School of Education, Hiroshima University, Higashi-Hiroshima 739-8524, Japan; orcid.org/0000-0002-1839-8163; Phone: +81-82-424-7092; Email: nkoga@hiroshima-u.ac.jp

Authors

Yasuhiro Sakai - Department of Science Education, Graduate School of Education, Hiroshima University, HigashiHiroshima 739-8524, Japan

Masahiro Fukuda - Department of Science Education, Graduate School of Education, Hiroshima University, Higashi-Hiroshima 739-8524, Japan

Daichi Hara - Department of Science Education, Graduate School of Education, Hiroshima University, HigashiHiroshima 739-8524, Japan

Yuu Tanaka - Department of Science Education, Graduate School of Education, Hiroshima University, HigashiHiroshima 739-8524, Japan

Loic Favergeon - Mines Saint-Etienne, University of Lyon, CNRS, UMR 5307 LGF, F-42023 Saint-Etienne, France; orcid.org/0000-0001-8181-867X

Notes

The authors declare no competing financial interest.

References

1.   Spencer, W. D.; Topley, B., CCCLIV. Chemical Kinetics of the System $Ag_2CO_3 = Ag_2O + CO_2$. *J. Chem. Soc.* **1929**, 2633-2650.
2.   Zawadzki, J.; Bretsznajder, S., Some Remarks on the Mechanism of Reactions of the Type: Solid=Solid + Gas. *Trans. Faraday Soc.* **1938**, *34*, 951-959.
3.   Hyatt, E. P.; Cutler, I. B.; Wadsworth, M. E., Calcium Carbonate Decomposition in Carbon Dioxide Atmosphere. *J. Am. Ceram. Soc.* **1958**, *41*, 70-74.
4.   Ingraham, T. R.; Marier, P., Kinetic Studies on the Thermal Decomposition of Calcium Carbonate. *Can. J. Chem. Eng.* **1963**, *41*, 170-173.
5.   Searcy, A. W.; Beruto, D., Kinetics of Endothermic Decomposition Reactions. 2. Effects of the Solid and Gaseous Products. *J. Phys. Chem.* **1978**, *82*, 163-167.
6.   Criado, J. M.; Gonzalez, F.; Gonzalez, M., Influence of the CO_2 Pressure on the Kinetics of Thermal Decomposition of Manganese Carbonate. *J. Therm. Anal.* **1982**, *24*, 59-65.

7.   Maciejewski, M.; Bałdyga, J., The Influence of the Pressure of the Gaseous Product on the Reversible Thermal Decomposition of Solids. *Thermochim. Acta* **1985**, *92*, 105-108.

8.   Criado, J. M.; González, M.; Macias, M., Influence of CO_2 Pressure on the Kinetics of Thermal Decomposition of $CdCO_3$. *Thermochim. Acta* **1987**, *113*, 31-38.

9.   Reading, M.; Dollimore, D.; Whitehead, R., The Measurement of Meaningful Kinetic Parameters for Solid State Decomposition Reactions. *J. Therm. Anal.* **1991**, *37*, 2165-2188.

10.   Criado, J. M.; González, M.; Macías, M., Influence of CO_2 Pressure on the Kinetics of Thermal Decomposition of Pbco3. *Thermochim. Acta* **1987**, *113*, 39-47.

11.   Criado, J.; González, M.; Málek, J.; Ortega, A., The Effect of the CO_2 Pressure on the Thermal Decomposition Kinetics of Calcium Carbonate. *Thermochim. Acta* **1995**, *254*, 121-127.

12.   Khinast, J.; Krammer, G. F.; Brunner, C.; Staudinger, G., Decomposition of Limestone: The Influence of CO_2 and Particle Size on the Reaction Rate. *Chem. Eng. Sci.* **1996**, *51*, 623-634.

13.   Bouineau, V.; Pijolat, M.; Soustelle, M., Characterisation of the Chemical Reactivity of a Caco3 Powder for Its Decomposition. *J. Europ. Ceram. Soc.* **1998**, *18*, 1319-1324.

14.   Koga, N.; Criado, J. M., The Influence of Mass Transfer Phenomena on the Kinetic Analysis for the Thermal Decomposition of Calcium Carbonate by Constant Rate Thermal Analysis (CRTA) under Vacuum. *Int. J. Chem. Kinet.* **1998**, *30*, 737-744.

15.   Yamada, S.; Koga, N., Kinetics of the Thermal Decomposition of Sodium Hydrogen Carbonate Evaluated by Controlled Rate Evolved Gas Analysis Coupled with Thermogravimetry. *Thermochim. Acta* **2005**, *431*, 38-43.

16.   Yamada, S.; Tsukumo, E.; Koga, N., Influences of Evolved Gases on the Thermal Decomposition of Zinc Carbonate Hydroxide Evaluated by Controlled Rate Evolved Gas Analysis Coupled with Tg. *J. Therm. Anal. Calorim.* **2009**, *95*, 489-493.

17.   Benton, A. F.; Drake, L. C., Kinetics of Reaction and Adsorption in the System Silver–Oxygen. *J. Am. Chem. Soc.* **1934**, *56*, 255-263.

18.   Vyazovkin, S., Kinetic Effects of Pressure on Decomposition of Solids. *Int. Rev. Phys. Chem.* **2020**, *39*, 35-66.

19.   Deutsch, M.; Birkelbach, F.; Knoll, C.; Harasek, M.; Werner, A.; Winter, F., An Extension of the NPK Method to Include the Pressure Dependency of Solid State Reactions. *Thermochim. Acta* **2017**, *654*, 168-178.

20.   Koga, N.; Favergeon, L.; Kodani, S., Impact of Atmospheric Water Vapor on the Thermal Decomposition of Calcium Hydroxide: A Universal Kinetic Approach to a Physico-Geometrical Consecutive Reaction in Solid-Gas Systems under Different Partial Pressures of Product Gas. *Phys. Chem. Chem. Phys.* **2019**, *21*, 11615-11632.

21.   Fukuda, M.; Favergeon, L.; Koga, N., Universal Kinetic Description for Thermal Decomposition of Copper(II) Hydroxide over Different Water Vapor Pressures. *J. Phys. Chem. C* **2019**, *123*, 20903-20915.

22.   Kodani, S.; Favergeon, L.; Koga, N., Revealing the Effect of Water Vapor Pressure on the Kinetics of Thermal Decomposition of Magnesium Hydroxide. *Phys. Chem. Chem. Phys.* **2020**, *22*.

23.   Yamamoto, Y.; Favergeon, L.; Koga, N., Thermal Dehydration of Lithium Sulfate Monohydrate Revisited with Universal Kinetic Description over Different Temperatures and Atmospheric Water Vapor Pressures. *J. Phys. Chem. C* **2020**, *124*, 11960-11976.

24.   Šesták, J., Diagnostic Limits of Phenomenological Kinetic Models Introducing the Accommodation Function. *J. Therm. Anal.* **1990**, *36*, 1997-2007.

25.   Koga, N., Physico-Geometric Kinetics of Solid-State Reactions by Thermal Analyses. *J. Therm. Anal.* **1997**, *49*, 45-56.

26.   Koga, N.; Tanaka, H., A Physico-Geometric Approach to the Kinetics of Solid-State Reactions as Exemplified by the Thermal Dehydration and Decomposition of Inorganic Solids. *Thermochim. Acta* **2002**, *388*, 41-61.

27.   Koga, N., Ozawa's Kinetic Method for Analyzing Thermoanalytical Curves. *J. Therm. Anal. Calorim.* **2013**, *113*, 1527-1541.

28.   Koga, N.; Šesták, J.; Simon, P., Some Fundamental and Historical Aspects of Phenomenological Kinetics in the Solid State Studied by Thermal Analysis. In *Thermal Analysis of Micro, Nano- and Non-Crystalline Materials*, Sestak, J.; Simon, P., Eds. Springer: 2013; pp 1-28.

29.   Koga, N., Physico-Geometric Approach to the Kinetics of Overlapping Solid-State Reactions. In *Handbook of Thermal Analysis and Calorimetry*, 2nd ed.; Vyazovkin, S.; Koga, N.; Schick, C., Eds. Elsevier: Amsterdam, 2018; Vol. 6, pp 213-251.

30.   Barret, P., Expression théOrique En Fonction De La Pression De La Loi De Vitesse De Croissance D'une Couche Non Protectrice ForméE Par DéComposition Thermique D'un Solide. *C. R. Acad. Sci. Paris, Serie C* **1968**, *266*, 856-859.

31.   Koga, N.; Criado, J. M.; Tanaka, H., Apparent Kinetic Behavior of the Thermal Decomposition of Synthetic Malachite. *Thermochim. Acta* **1999**, *340-341*, 387-394.

32.   Gotor, F. J.; Criado, J. M.; Malek, J.; Koga, N., Kinetic Analysis of Solid-State Reactions: The Universality of Master Plots for Analyzing Isothermal and Nonisothermal Experiments. *J. Phys. Chem. A* **2000**, *104*, 10777-10782.

33.   Koga, N.; Yamada, S., Influences of Product Gases on the Kinetics of Thermal Decomposition of Synthetic Malachite Evaluated by Controlled Rate Evolved Gas Analysis Coupled with Thermogravimetry. *Int. J. Chem. Kinet.* **2005**, *37*, 346-354.

34.   Koga, N.; Tatsuoka, T.; Tanaka, Y., Effect of Atmosphericwater Vapor on the Kinetics of Thermal Decomposition of Copper(II) Carbonate Hydroxide. *J. Therm. Anal. Calorim.* **2009**, *95*, 483-487.

35.   Koga, N.; Tatsuoka, T.; Tanaka, Y.; Yamada, S., Catalytic Action of Atmospheric Water Vapor on the Thermal Decomposition of Synthetic Hydrozincite. *Trans. Mater. Soc* **2009**, *34*, 343-346.

36.   Berger, E. E., Effect of Steam on the Decomposition of Limestone. *Ind. Eng. Chem. Res.* **1927**, *19*, 594-596.

37.   MacIntire, W. H.; Stansel, T. B., Steam Catalysis in Calcinations of Dolomite and Limestone Fines. *Ind. Eng. Chem. Res.* **1953**, *45*, 1548-1555.

38.   Burnham, A. K.; Stubblefield, C. T.; Campbell, J. H., Effects of Gas Environment on Mineral Reactions in Colorado Oil Shale. *Fuel* **1980**, *59*, 871-877.

39.   Wang, Y.; Thomson, W. J., The Effects of Steam and Carbon Dioxide on Calcite Decomposition Using Dynamic X-Ray Diffraction. *Chem. Eng. Sci.* **1995**, *50*, 1373-1382.

40.   Yin, J.; Kang, X.; Qin, C.; Feng, B.; Veeraragavan, A.; Saulov, D., Modeling of $CaCO_3$ Decomposition under Co_2/H_2o Atmosphere in Calcium Looping Processes. *Fuel Process. Technol.* **2014**, *125*, 125-138.

41.   Guo, S.; Wang, H.; Liu, D.; Yang, L.; Wei, X.; Wu, S., Understanding the Impacts of Impurities and Water Vapor on Limestone Calcination in a Laboratory-Scale Fluidized Bed. *Energy Fuels* **2015**, *29*, 7572-7583.

42.   Valverde, J. M.; Medina, S., Limestone Calcination under Calcium-Looping Conditions for Co_2 Capture and Thermochemical Energy Storage in the Presence of H_2O: An in Situ XRD Analysis. *Phys. Chem. Chem. Phys.* **2017**, *19*, 7587-7596.

43.   Giammaria, G.; Lefferts, L., Catalytic Effect of Water on Calcium Carbonate Decomposition. *J. CO2 Util.* **2019**, *33*, 341-356.

44.   He, D.; Ou, Z.; Qin, C.; Deng, T.; Yin, J.; Pu, G., Understanding the Catalytic Acceleration Effect of Steam on $Caco_3$ Decomposition by Density Function Theory. *Chem. Eng. J.* **2020**, *379*.

45.   Kokes, R. J.; Glemza, R., Thermodynamics of Adsorption of Carbon Dioxide on Zinc Oxide. *J. Phys. Chem.* **1965**, *69*, 17-21.

46.   Sawada, Y.; Murakami, M.; Nishide, T., Thermal Analysis of Basic Zinc Carbonate. Part 1. Carbonation Process of Zinc Oxide Powders at 8 and 13°C. *Thermochim. Acta* **1996**, *273*, 95-102.

47.   Lindén, I.; Backman, P.; Brink, A.; Hupa, M., Influence of Water Vapor on Carbonation of Cao in the Temperature Range 400–550°C. *Ind. Eng. Chem. Res.* **2011**, *50*, 14115-14120.

48.   Koga, N.; Kodani, S., Thermally Induced Carbonation of $Ca(OH)_2$ in a CO_2 Atmosphere: Kinetic Simulation of Overlapping Mass-Loss and Mass-Gain Processes in a Solid-Gas System. *Phys. Chem. Chem. Phys.* **2018**, *20*, 26173-26189.

49.   Torres-Rodríguez, D. A.; Pfeiffer, H., Thermokinetic Analysis of the MgO Surface Carbonation Process in the Presence of Water Vapor. *Thermochim. Acta* **2011**, *516*, 74-78.

50.   Fagerlund, J.; Highfield, J.; Zevenhoven, R., Kinetics Studies on Wet and Dry Gas–Solid Carbonation of Mgo and $Mg(OH)_2$ for CO_2 Sequestration. *RSC Adv.* **2012**, *2*.

51. Hamdi, S.; Vieille, L.; Nahdi, K.; Favergeon, L., Synthesis, Characterization and Low-Temperature Carbonation of Mesoporous Magnesium Oxide. *J. Therm. Anal. Calorim.* **2019**, *138*, 1923-1933.

52. Stanmore, B. R.; Gilot, P., Review—Calcination and Carbonation of Limestone During Thermal Cycling for CO_2 Sequestration. *Fuel Process. Technol.* **2005**, *86*, 1707-1743.

53. Manovic, V.; Anthony, E. J., Lime-Based Sorbents for High-Temperature CO_2 Capture–a Review of Sorbent Modification Methods. *Int. J. Environ. Res. Public Health* **2010**, *7*, 3129-40.

54. Samanta, A.; Zhao, A.; Shimizu, G. K. H.; Sarkar, P.; Gupta, R., Post-Combustion CO_2 Capture Using Solid Sorbents: A Review. *Ind. Eng. Chem. Res.* **2011**, *51*, 1438-1463.

55. Galwey, A. K.; Brown, M. E., *Thermal Decomposition of Ionic Solids*; Elsevier: Amsterdam, 1999.

56. Galwey, A. K., Structure and Order in Thermal Dehydrations of Crystalline Solids. *Thermochim. Acta* **2000**, *355*, 181-238.

57. Methivier, A.; Pijolat, M., Thermal-Stability of Zirconia as a Catalyst Support: Kinetics and Modeling. *J. Catal.* **1993**, *139*, 329-337.

58. Tatsuoka, T.; Koga, N., Effect of Atmospheric Water Vapor on the Thermally Induced Crystallization in Zirconia Gel. *J. Am. Ceram. Soc.* **2012**, *95*, 557-564.

59. Anderson, P. J.; Morgan, P. L., Effects of Water Vapour on Sintering of MgO. *Trans. Faraday Soc.* **1964**, *60*, 930-937.

60. Eastman, P. F.; Cutler, I. B., Effect of Water Vapor on Initial Sintering of Magnesia. *J. Am. Ceram. Soc.* **1966**, *49*, 526-530.

61. Beruto, D.; Botter, R.; Searcy, A. W., H_2O-Catalyzed Sintering of ~2-nm-Cross- Section Particles of MgO. *J. Am. Ceram. Soc.* **1987**, *70*, 155-159.

62. Hebrard, J.-L.; Nortier, P.; Pijolat, M.; Soustelle, M., Initial Sintering of Submicrometer Titania Anatase Powder. *J. Am. Ceram. Soc.* **1990**, *73*, 79-84.

63. Frost, R. L.; Ding, Z.; Kloprogge, J. T.; Martens, W. N., Thermal Stability of Azurite and Malachite in Relation to the Formation of Mediaeval Glass and Glazes. *Thermochim. Acta* **2002**, *390*, 133-144.

64. Kanari, N.; Mishra, D.; Gaballah, I.; Dupré, B., Thermal Decomposition of Zinc Carbonate Hydroxide. *Thermochim. Acta* **2004**, *410*, 93-100.

65. Özgür, Ü.; Alivov, Y. I.; Liu, C.; Teke, A.; Reshchikov, M. A.; Doğan, S.; Avrutin, V.; Cho, S. J.; Morkoç, H., A Comprehensive Review of Zno Materials and Devices. *J. Appl. Phys.* **2005**, *98*.

66. Frost, R. L.; Martens, W. N.; Wain, D. L.; Hales, M. C., Infrared and Infrared Emission Spectroscopy of the Zinc Carbonate Mineral Smithsonite. *Spectrochim. Acta, Part A* **2008**, *70*, 1120-6.

67. Garcia-Guinea, J.; Crespo-Feo, E.; Correcher, V.; Rubio, J.; Roux, M. V.; Townsend, P. D., Thermo-Optical Detection of Defects and Decarbonation in Natural Smithsonite. *Phys. Chem. Miner.* **2009**, *36*, 431-438.

68. Frost, R. L.; Hales, M. C.; Wain, D. L., Raman Spectroscopy of Smithsonite. *J. Raman Spectrosc.* **2008**, *39*, 108-114.

69. Gotor, F. J.; Macas, M.; Ortega, A.; Criado, J. M., Simultaneous Use of Isothermal, Nonisothermal, and Constant Rate Thermal Analysis (CRTA) for Discerning the Kinetics of the Thermal Dissociation of Smithsonite. *Int. J. Chem. Kinet.* **1998**, *30*, 647-655.

70. Budrugeac, P.; Criado, J. M.; Gotor, F. J.; Popescu, C.; Segal, E., Kinetic Analysis of Dissociation of Smithsonite from a Set of Non-Isothermal Data Obtained at Different Heating Rates. *J. Therm. Anal. Calorim.* **2001**, *63*, 777-786.

71. Hales, M. C.; Frost, R. L., Synthesis and Vibrational Spectroscopic Characterisation of Synthetic Hydrozincite and Smithsonite. *Polyhedron* **2007**, *26*, 4955-4962.

72. Hales, M. C.; Frost, R. L., Thermal Analysis of Smithsonite and Hydrozincite. *J. Therm. Anal. Calorim.* **2008**, *91*, 855-860.

73. Vágvölgyi, V.; Hales, M.; Martens, W.; Kristóf, J.; Horváth, E.; Frost, R. L., Dynamic and Controlled Rate Thermal Analysis of Hydrozincite and Smithsonite. *J. Therm. Anal. Calorim.* **2008**, *92*, 911-916.

74. Brunauer, S.; Emmett, P. H.; Teller, E., Adsorption of Gases in Multimolecular Layers. *J. Am. Chem. Soc.* **1938**, *60*, 309-319.

75.   Toft Sorensen, O. T.; Rouquerol, J., *Sample Controlled Thermal Analysis*; Kluwer: Dordrecht, 2003.

76.   Criado, J. M.; Perez-Maqueda, L. A.; Koga, N., Sample Controlled Thermal Analysis (SCTA) as a Promising Tool for Kinetic Characterization of Solid-State Reaction and Controlled Material Synthesis. In *Thermal Physics and Thermal Analysis*, Šesták, J.; Hubík, P.; Mareš, J. J., Eds. Springer Nature: Switzerland, 2017; pp 11-43.

77.   Graf, D. L., Crystallographic Tables for the Rhombohedral Carbonates. *Am. Mineral* **1961**, *46*, 1283-1316.

78.   Effenberger, H.; Mereiter, K.; Zemann, J., Crystal Structure Refinements of Magnesite, Calcite, Rhodochrosite, Siderite, Smithonite, and Dolomite, with Discussion of Some Aspects of the Stereochemistry of Calcite Type Carbonates. *Z. Krist.* **1981**, *156*.

79.   Garciamartinez, O.; Rojas, R.; Vila, E.; Devidales, J., Microstructural Characterization of Nanocrystals of Zno and Cuo Obtained from Basic Salts. *Solid State Ionics* **1993**, *63-65*, 442-449.

80.   Patterson, A. L., The Scherrer Formula for X-Ray Particle Size Determination. *Phys. Rev.* **1939**, *56*, 978-982.

81.   Friedman, H. L., Kinetics of Thermal Degradation of Cha-Forming Plastics from Thermogravimetry, Application to a Phenolic Plastic. *J. Polym. Sci., Part C* **1964**, *6*, 183-195.

82.   Ozawa, T., Kinetic Analysis of Derivative Curves in Thermal Analysis. *J. Therm. Anal.* **1970**, *2*, 301-324.

83.   Ozawa, T., Applicability of Friedman Plot. *J. Therm. Anal.* **1986**, *31*, 547-551.

84.   Málek, J., The Kinetic Analysis of Non-Isothermal Data. *Thermochim. Acta* **1992**, *200*, 257-269.

85.   Koga, N., Kinetic Analysis of Thermoanalytical Data by Extrapolating to Infinite Temperature. *Thermochim. Acta* **1995**, *258*, 145-159.

86.   Gotor, F. J.; Criado, J. M.; Málek, J.; Koga, N., Kinetic Analysis of Solid-State Reactions: The Universality of Master Plots for Analyzing Isothermal and Nonisothermal Experiments. *J. Phys. Chem. A* **2000**, *104*, 10777-10782.

87.   Criado, J. M.; Perez-Maqueda, L. A.; Gotor, F. J.; Málek, J.; Koga, N., A Unified Theory for the Kinetic Analysis of Solid State Reactions under Any Thermal Pathway. *J. Therm. Anal. Calorim.* **2003**, *72*, 901-906.

88.   Ozawa, T., A New Method of Analyzing Thermogravimetric Data. *Bull. Chem. Soc. Jpn.* **1965**, *38*, 1881-1886.

89.   Ozawa, T., Non-Isothermal Kinetics and Generalized Time. *Thermochim. Acta* **1986**, *100*, 109-118.

90.   Šesták, J.; Berggren, G., Study of the Kinetics of the Mechanism of Solid-State Reactions at Increasing Temperatures. *Thermochim. Acta* **1971**, *3*, 1-12.

91.   Šesták, J., Rationale and Fallacy of Thermoanalytical Kinetic Patterns. *J. Therm. Anal. Calorim.* **2011**, *110*, 5-16.

92.   Johnson, W. A.; Mehl, K. F., Reaction Kinetics in Processes of Nucleation and Growth. *Trans. Am. Inst. Min. Metall. Eng.* **1939**, *135*, 416-458.

93.   Avrami, M., Kinetics of Phase Change. I. General Theory. *J. Chem. Phys.* **1939**, *7*, 1103-1112.

94.   Avrami, M., Kinetics of Phase Change. II. Transformation-Time Relations for Random Distribution of Nuclei. *J. Chem. Phys.* **1940**, *8*, 212-223.

95.   Avrami, M., Kinetics of Phase Change. III. Granulation, Phase Change, and Microstructure. *J. Chem. Phys.* **1941**, *9*, 177-184.

96.   Koga, N.; Tanaka, H., A Kinetic Compensation Effect Established for the Thermal Decomposition of a Solid. *J. Therm. Anal.* **1991**, *37*, 347-363.

97.   Koga, N.; Šesták, J., Kinetic Compensation Effect as a Mathematical Consequence of the Exponential Rate Constant. *Thermochim. Acta* **1991**, *182*, 201-208.

98.   Koga, N.; Šesták, J., Further Aspects of the Kinetic Compensation Effect. *J. Therm. Anal.* **1991**, *37*, 1103-1108.

99.   Koga, N., A Review of the Mutual Dependence of Arrhenius Parameters Evaluated by the Thermoanalytical Study of Solid-State Reactions: The Kinetic Compensation Effect. *Thermochim. Acta* **1994**, *244*, 1-20.

100. Galwey, A. K.; Mortimer, M., Compensation Effects and Compensation Defects in Kinetic and Mechanistic Interpretations of Heterogeneous Chemical Reactions. *Int. J. Chem. Kinet.* **2006**, *38*, 464-473.

101. Xu, D.; Chai, M.; Dong, Z.; Rahman, M. M.; Yu, X.; Cai, J., Kinetic Compensation Effect in Logistic Distributed Activation Energy Model for Lignocellulosic Biomass Pyrolysis. *Bioresour. Technol.* **2018**, *265*, 139-145.

102. Kodani, S.; Koga, N., Kinetics of Contracting Geometry-Type Reactions in the Solid State: Implications from the Thermally Induced Transformation Processes of Alpha-Oxalic Acid Dihydrate. *Phys. Chem. Chem. Phys.* **2020**, *22*, 19560-19572.

103. Garner, W. E., The Kinetics of Endothermic Solid Reactions. In *Chemistry of the Solid State*, Garrner, W. E., Ed. Butterworths: London, 1955; pp 213-231.

104. Young, D. A., *Decomposition of Solids*; Pergamon: Oxford, 1966; Vol. 1.

105. Delmon, B., *Introduction a La Cinetique Heterogene*; Editions Technip: Paris, 1969.

106. Barret, P., *Cinetique Heterogene*; Gauthier-Villars: Paris, 1973.

107. Tompkins, F. C., Decomposition Reactions. In *Treates on Solid State Chemistry, Vol. 4 Reactivity of Solids*, Hannay, N. B., Ed. Plenum: New York, 1976; Vol. 4, pp 193-231.

108. Brown, M. E.; Dollimore, D.; Galwey, A. K., *Reactions in the Solid State*; Elsevier: Amsterdam, 1980; Vol. 22.

109. Yokokawa, H.; Yamauchi, S.; Matsumoto, T., The Thermodynamic Database Malt. *Calphad* **1999**, *23*, 357-364.

110. Yokokawa, H.; Yamauchi, S.; Matsumoto, T., Thermodynamic Database Malt for Windows with Gem and Chd. *Calphad* **2002**, *26*, 155-166.

111. Kröger, F. A., *The Chemistry of Imperfect Crystals: Vol.2, Imperfection Chemistry of Crystalline Solids*; North-Holland Publishing Company: Amsterdam, 1974.

112. Mampel, K. L., Time Conversion Formulas for Heterogeneous Reactions at the Phase Boundaries of Solid Bodies, I: The Development of the Mathematical Method and the Derivation of Area Conversion Formulas. *Z. Phys. Chem. Abt. A* **1940**, *187*, 43-57

113. Favergeon, L.; Pijolat, M.; Soustelle, M., Surface Nucleation and Anisotropic Growth Models for Solid-State Reactions. *Thermochim. Acta* **2017**, *654*, 18-27.

114. Ogasawara, H.; Koga, N., Kinetic Modeling for Thermal Dehydration of Ferrous Oxalate Dihydrate Polymorphs: A Combined Model for Induction Period-Surface Reaction-Phase Boundary Reaction. *The journal of physical chemistry. A* **2014**, *118*, 2401-12.

115. Achar, B. B.; Brindley, G. W.; Sharp, J. H. In *Thermal Decomposition Kinetics of Some New Unsaturated Polyesters*, Proceedings of International Clay Conference, Jersalem, Heller, W., Ed. Jersalem, 1966; p 67.